

A terrestrial planet candidate in a temperate orbit around Proxima Centauri

Guillem Anglada-Escudé¹, Pedro J. Amado², John Barnes³, Zaira M. Berdiñas², R. Paul Butler⁴, Gavin A. L. Coleman¹, Ignacio de la Cueva⁵, Stefan Dreizler⁶, Michael Endl⁷, Benjamin Giesers⁶, Sandra V. Jeffers⁶, James S. Jenkins⁸, Hugh R. A. Jones⁹, Marcin Kiraga¹⁰, Martin Kürster¹¹, María J. López-González², Christopher J. Marvin⁶, Nicolás Morales², Julien Morin¹², Richard P. Nelson¹, José L. Ortiz², Aviv Ofir¹³, Sijme-Jan Paardekooper¹, Ansgar Reiners⁶, Eloy Rodríguez², Cristina Rodríguez-López², Luis F. Sarmiento⁶, John P. Strachan¹, Yiannis Tsapras¹⁴, Mikko Tuomi⁹ & Mathias Zechmeister⁶

At a distance of 1.295 parsecs¹, the red dwarf Proxima Centauri (α Centauri C, GL 551, HIP 70890 or simply Proxima) is the Sun's closest stellar neighbour and one of the best-studied low-mass stars. It has an effective temperature of only around 3,050 kelvin, a luminosity of 0.15 per cent of that of the Sun, a measured radius of 14 per cent of the radius of the Sun² and a mass of about 12 per cent of the mass of the Sun. Although Proxima is considered a moderately active star, its rotation period is about 83 days (ref. 3) and its quiescent activity levels and X-ray luminosity⁴ are comparable to those of the Sun. Here we report observations that reveal the presence of a small planet with a minimum mass of about 1.3 Earth masses orbiting Proxima with a period of approximately 11.2 days at a semi-major-axis distance of around 0.05 astronomical units. Its equilibrium temperature is within the range where water could be liquid on its surface⁵.

The results presented here consist of an analysis of previously obtained Doppler measurements (pre-2016 data) and the confirmation of a signal in a specifically designed follow-up campaign in 2016. The Doppler data come from two precision radial velocity instruments, both at the European Southern Observatory (ESO): the High Accuracy Radial velocity Planet Searcher (HARPS) and the Ultraviolet and Visual Echelle Spectrograph (UVES). HARPS is a high-resolution stabilized echelle spectrometer installed at the ESO 3.6 m telescope (La Silla Observatory, Chile), the wavelength of which is calibrated using hollow cathode lamps (ThAr). HARPS has demonstrated radial velocity measurements at approximately 1 m s^{-1} precision over timescales of years⁶, including measurements of low-mass stars⁷. All of the HARPS spectra were extracted and calibrated with the standard ESO Data Reduction Software and radial velocities were measured using a least-squares template matching technique⁷. HARPS data are separated into two data sets. The first set includes all of the data obtained before 2016 by several programmes (HARPS pre-2016). The second HARPS set comes from the more recent Pale Red Dot campaign (PRD hereafter), which was designed to eliminate period ambiguities using new HARPS observations and quasi-simultaneous photometry. The HARPS PRD observations consisted of one spectrum obtained almost every night between 19 January and 31 March 2016. The UVES observations used the iodine cell technique⁸ and were obtained in the framework of the UVES survey for terrestrial planets around M-class dwarfs between 2000 and 2008. The spectra were extracted using the standard procedures of the UVES survey⁹ and new radial velocities were obtained using up-to-date iodine

reduction codes¹⁰. As systematic calibration errors produce correlations among the observations for each night¹¹, we consolidated the Doppler measurements through nightly averages to present a simpler and more conservative signal search. This led to 72 UVES, 90 HARPS pre-2016 and 54 HARPS PRD epochs. The PRD photometric observations were obtained using the Astrograph for the South Hemisphere II telescope (ASH2 hereafter¹², with S II and H α narrowband filters) and the Las Cumbres Observatory Global Telescope network¹³ (with Johnson B and V band filters), over the same time interval and similar sampling rates as the HARPS PRD observations. Further details about each campaign and the photometry are detailed in Methods. All of the time series used in this work are available as Supplementary Data.

The search and assessment of the statistical significance (see below and Methods for more details) of the signals were performed using frequentist¹⁴ and Bayesian¹⁵ methods. The periodograms in Fig. 1 represent the improvement of a reference statistic as a function of trial period, with the peaks representing the most probable new signals. The improvement in the logarithm of the likelihood function $\Delta \ln L$ is the reference statistic used in the frequentist framework, and its value is then used to assess the false-alarm probability (FAP) of the detection¹⁴. An FAP below 1% is considered suggestive of periodic variability, and anything below 0.1% is considered to be a significant detection. In the Bayesian framework, the signals are first searched using a specialized sampling method¹⁶ that enables the exploration of multiple local maxima of the posterior density (the result of this process is the red lines in Fig. 1), and the significance of the signals is then assessed by obtaining the ratios of evidences of the models. In a Bayesian context, the evidence B_m of a model m is the integral of its Bayesian posterior density. A more detailed description and references are provided in Methods. If the evidence ratio between two models exceeds some threshold (for example, $B_1/B_0 > 10^3$), then the model in the numerator (with one planet) is favoured against the model in the denominator (no planet).

An isolated peak at about 11.2 d was recovered when all of the night averages in the pre-2016 data sets were averaged (Fig. 1a). Despite the significance of the signal, the analysis of the pre-2016 subsets produced slightly different periods depending on the noise assumptions and which of the subsets were considered. Confirmation or refutation of this signal at 11.2 d was the main driver for the proposal of the HARPS PRD campaign. The analysis of the HARPS PRD data revealed a single significant signal at approximately the same 11.3 ± 0.1 d period (Fig. 1b), but this period coincidence alone does not prove consistency with

¹School of Physics and Astronomy, Queen Mary University of London, 327 Mile End Road, London E1 4NS, UK. ²Instituto de Astrofísica de Andalucía – Consejo Superior de Investigaciones Científicas, Glorieta de la Astronomía S/N, E-18008 Granada, Spain. ³Department of Physical Sciences, Open University, Walton Hall, Milton Keynes MK7 6AA, UK. ⁴Carnegie Institution of Washington, Department of Terrestrial Magnetism, 5241 Broad Branch Road NW, Washington DC 20015, USA. ⁵Astroimagen, C. Abad y Lasierra, 58 Bis, 6-2, 07800 Ibiza, Spain. ⁶Institut für Astrophysik, Georg-August-Universität Göttingen, Friedrich-Hund-Platz 1, 37077 Göttingen, Germany. ⁷McDonald Observatory, the University of Texas at Austin, 2515 Speedway, C1400, Austin, Texas 78712, USA. ⁸Departamento de Astronomía, Universidad de Chile, Camino El Observatorio 1515, Las Condes, Santiago, Chile. ⁹Centre for Astrophysics Research, Science & Technology Research Institute, University of Hertfordshire, Hatfield AL10 9AB, UK. ¹⁰Warsaw University Observatory, Aleje Ujazdowskie 4, Warszawa, Poland. ¹¹Max-Planck-Institut für Astronomie, Königstuhl 17, 69117 Heidelberg, Germany. ¹²Laboratoire Univers et Particules de Montpellier, Université de Montpellier, Place E. Bataillon—CC 72, 34095 Montpellier Cédex 05, France. ¹³Department of Earth and Planetary Sciences, Weizmann Institute of Science, 234 Herzl Street, Rehovot 76100, Israel. ¹⁴Astronomisches Rechen-Institut, Mönchhofstrasse 12–14, 69120 Heidelberg, Germany.

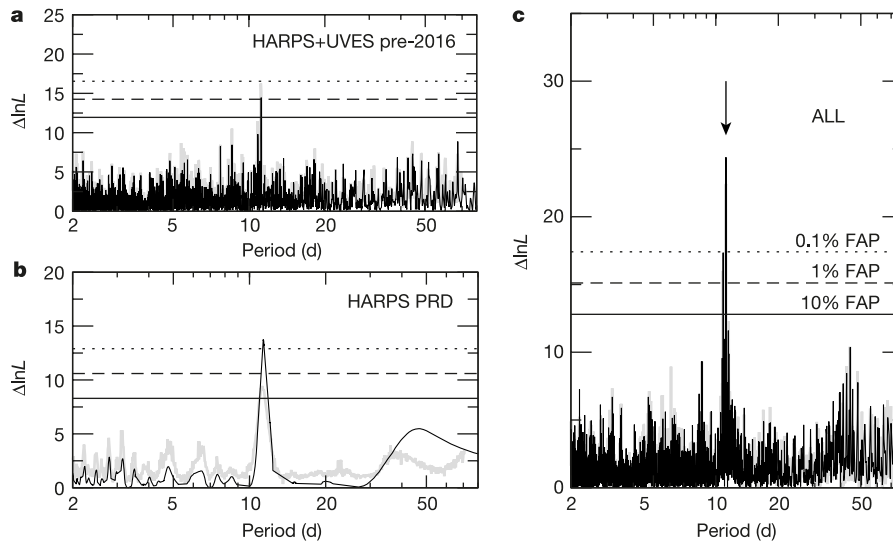


Figure 1 | Detection of a Doppler signal at 11.2 d. **a, b,** Detection periodograms of the 11.2 d signal in the HARPS+UVES pre-2016 data (**a**) and the HARPS PRD campaign only (**b**). **c,** The periodogram obtained after combining all of the data sets. Black lines correspond to the Δ

of the pre-2016 data. Final confirmation is achieved when all of the data sets are combined (Fig. 1c)—the statistical significance of the signal at 11.2 d then increases dramatically (FAP < 10^{-7} , Bayesian evidence ratio $B_1/B_0 > 10^6$). This implies that not only the period, but also the amplitude and phase are consistent during the 16 years of accumulated observations (see Fig. 2). All of the analyses performed with and without correlated-noise models produced consistent results. A second signal in the range of 60–500 d was also detected, but its nature is still unclear due to stellar activity and inadequate sampling.

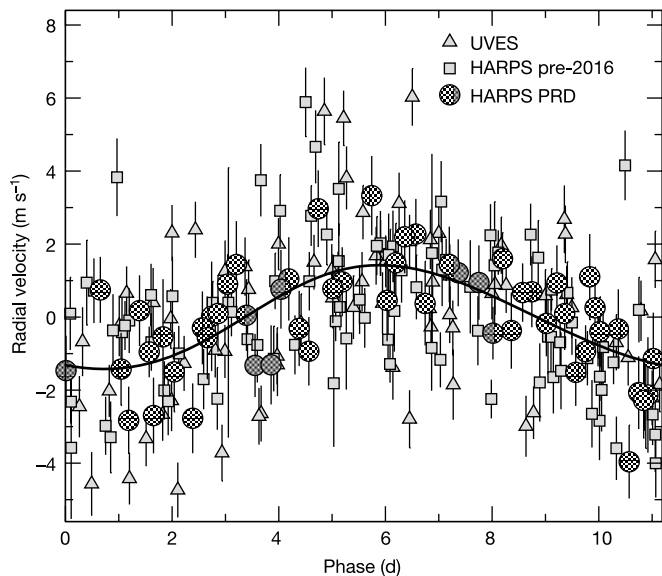


Figure 2 | All of the data sets phase-folded at the 11.2 d signal. Radial velocity measurements phase folded at the 11.2 d period of the planet candidate for 16 years of observations. The abscissa values of phase-folded plots are determined by first computing the difference between each Julian date and the reference epoch of the Keplerian fit (Julian date of the first UVES observation), and then computing the remainder of the division of this difference with the orbital period. Although its nature is unclear, a second signal at $P \approx 200$ d was fitted and subtracted from the data to produce this plot and improve visualization. Circles correspond to HARPS PRD, triangles are HARPS pre-2016 and squares are UVES. The black line represents the best Keplerian fit to this phase folded representation of the data. Error bars correspond to formal 1σ uncertainties.

$\Delta \ln L$ statistic, whereas the grey thick lines represent the logarithm of the Bayesian posterior density (see text, arbitrary vertical offset applied for visual comparison of the two statistics). The horizontal solid, dashed and dotted lines represent the FAP thresholds of the frequentist analysis.

Stellar variability can cause spurious Doppler signals that mimic planetary candidates, especially when combined with uneven sampling^{9,17}. To address this, the time series of the photometry and spectroscopic activity indices were also searched for signals. After removing occasional flares, all four photometric time series show the same clear modulation with a period of $P \approx 80$ days (Fig. 3b–e), which is consistent with the previously reported photometric period of approximately 83 d (ref. 3). Spectroscopic activity indices were measured on all of the HARPS spectra, and their time series were also investigated. The width of the spectral lines (measured as the variance of the mean line, or m_2) follows a time dependence that is almost identical to the light curves, a behaviour that has already been reported for other M dwarf stars¹⁸. The time series of the indices that are based on chromospheric emission lines (for example, $H\alpha$) do not show evidence of periodic variability, even after removing the data points that are likely to be affected by flares. We also investigated possible correlations of the Doppler measurements with the activity indices by including linear correlation terms in the Bayesian model of the Doppler data. Although some indices do show hints of correlation in some campaigns, including them in the model produces lower probabilities, owing to overparameterization. Flares have very little effect on our Doppler velocities, as has already been suggested by previous observations of Proxima¹⁹. More details are provided in Methods and Extended Data Fig. 8. As the analysis of the activity data failed to identify any stellar activity feature that is likely to generate a spurious Doppler signal at 11.2 d, we conclude that the variability in the data is best explained by the presence of a planet (Proxima b, hereafter) orbiting the star. All of the available photometric light curves were searched for evidence of transits, but no obvious transit-like features were detectable in our light curves. We used optimal box-Least-Squares codes²⁰ to search for candidate signals in data from the All Sky Automatic Survey³. No significant transit signal was found down to a depth of about 5%. The most likely orbital solution and the putative properties of the planet and transits are given in Table 1.

The Doppler semi-amplitude of Proxima b (approximately 1.4 m s^{-1}) is not particularly small compared with other reported planet candidates⁶. The uneven and sparse sampling combined with the longer-term variability of the star seem to be the reasons why the signal could not be unambiguously confirmed with pre-2016 data rather than the total amount of data accumulated. The corresponding minimum planetary mass is about 1.3 Earth masses (M_{\oplus}). With a semi-major axis of approximately 0.05 AU, it lies squarely in the centre of the classical habitable zone for Proxima⁵. As mentioned earlier, the presence of another

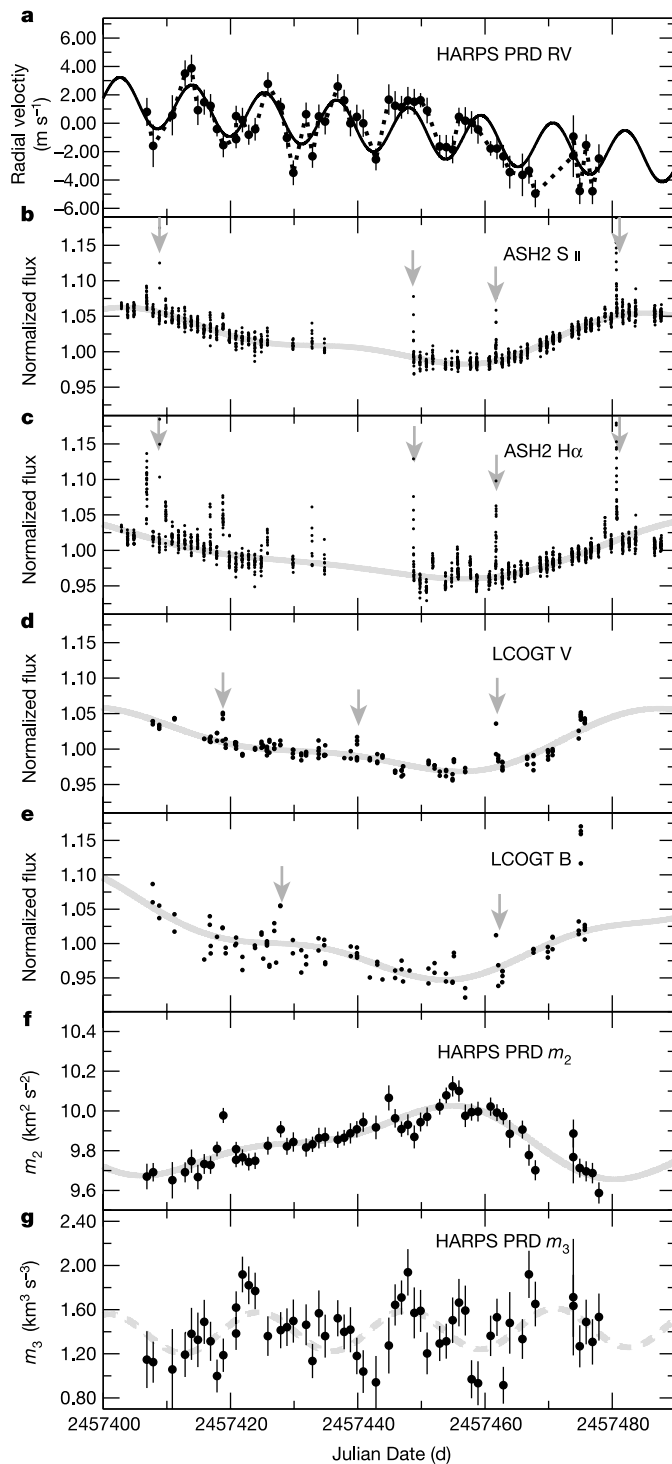


Figure 3 | Time series obtained during the PRD campaign. **a**, HARPS-PRD radial velocity measurements. **b**, **c**, Quasi-simultaneous photometry from ASH2 for S II (**b**) and H α (**c**). **d**, **e**, Quasi-simultaneous photometry from LCOGT for V (**d**) and B (**e**). **f**, **g**, Central moments of the mean line profiles for m_2 (**f**) and m_3 (**g**). The solid lines show the best fits. A dashed line indicates a signal that is not sufficiently statistically significant. Excluded measurements that probably affected activity events (for example, flares) are marked with grey arrows. The photometric time series and m_2 show evidence of the same approximately 80 d modulation. Error bars correspond to formal 1σ uncertainties.

super- M_{\oplus} planet cannot yet be ruled out at longer orbital periods and Doppler semi-amplitudes of $<3\text{ m s}^{-1}$. By numerical integration of some putative orbits, we verified that the presence of such a planet would not compromise the orbital stability of Proxima b.

Table 1 | Stellar properties, Keplerian parameters, and derived quantities

Stellar properties	Value	Reference
Spectral type	M5.5V	2
M_*/M_{\odot}	0.120 (0.105–0.135)	30
R_*/R_{\odot}	0.141 (0.120–0.162)	2
L_*/L_{\odot}	0.00155 (0.00149–0.00161)	2
Effective temperature (K)	3,050 (2,950–3,150)	2
Rotation period (d)	about 83	3
Habitable zone range (AU)	about 0.0423–0.0816	30
Habitable zone periods (d)	about 9.1–24.5	30
Keplerian fit		
Proxima b		
Period (d)	11.186 (11.184–11.187)	
Doppler amplitude (m s^{-1})	1.38 (1.17–1.59)	
Eccentricity, e	<0.35	
Mean longitude, $\lambda = \omega + M_0$ ($^{\circ}$)	110 (102–118)	
Argument of periastron, ω_0 ($^{\circ}$)	310 (0–360)	
Statistics summary		
Frequentist FAP	7×10^{-8}	
Bayesian odds in favour, B_1/B_0	2.1×10^7	
UVES jitter (m s^{-1})	1.69 (1.22–2.33)	
HARPS pre-2016 jitter (m s^{-1})	1.76 (1.22–2.36)	
HARPS PRD jitter (m s^{-1})	1.14 (0.57–1.84)	
Derived quantities		
Orbital semi-major axis, a (AU)	0.0485 (0.0434–0.0526)	
Minimum mass, $m_p \sin i$ (M_{\oplus})	1.27 (1.10–1.46)	
Equilibrium black body temperature (K)	234 (220–240)	
Irradiance compared with Earth	65%	
Geometric probability of transit	about 1.5%	
Transit depth (Earth-like density)	about 0.5%	

The estimates are the maximum *a posteriori* values and the uncertainties of the parameters are expressed as 68% credibility intervals. We provide only an upper limit for the eccentricity (95% confidence level). Extended Data Table 1 contains the list of all of the model parameters.

The habitability of planets like Proxima b—in the sense of sustaining an atmosphere and liquid water on its surface—is a matter of intense debate. The most common arguments against habitability are tidal locking, strong stellar magnetic fields, strong flares and high ultraviolet and X-ray fluxes; but none of these have been proved definitive. Tidal locking does not preclude a stable atmosphere via global atmospheric circulation and heat redistribution²¹. The average global magnetic flux density of Proxima is $600 \pm 150\text{ G}$ (ref. 22), which is quite large compared with that of the Sun (1 G). However, several studies have shown that planetary magnetic fields in tidally locked planets can be strong enough to prevent atmospheric erosion by stellar magnetic fields²³ and flares²⁴. Because of its close orbit to Proxima, Proxima b suffers from X-ray fluxes that are approximately 400 times that experienced by Earth, but studies of similar systems indicate that atmospheric losses can be relatively small²⁵. Further characterization of such planets can also inform us about the origin and evolution of terrestrial planets. For example, the formation of Proxima b from *in situ* disk material is implausible because disk models for small stars would contain less than $1M_{\oplus}$ of solids within a distance of 1 AU. There are three possibilities: the planet migrated in via type I migration²⁶; planetary embryos migrated in and coalesced at the current planet's orbit; or pebbles/small planetesimals migrated via aerodynamic drag²⁷ and later coagulated into a larger body. Although migrated planets and embryos that originate beyond the ice-line would be rich in volatiles, pebble migration would produce much drier worlds. A warm terrestrial planet orbiting Proxima offers the opportunity to attempt further characterization via transits (ongoing searches), by direct imaging and high-resolution spectroscopy in the next decades²⁸, and possibly robotic exploration in the coming centuries²⁹.

Online Content Methods, along with any additional Extended Data display items and Source Data, are available in the online version of the paper; references unique to these sections appear only in the online paper.

Received 6 May; accepted 7 July 2016.

- van Leeuwen, F. Validation of the new Hipparcos reduction. *Astron. Astrophys.* **474**, 653–664 (2007).
- Boyajian, T. S. *et al.* Stellar diameters and temperatures. II: Main-sequence K- and M-stars. *Astrophys. J.* **757**, 112 (2012).
- Kiraga, M. & Stepien, K. Age–rotation–activity relations for M dwarf stars. *Acta Astron.* **57**, 149–172 (2007).
- Güdel, M., Audard, M., Reale, F., Skinner, S. L. & Linsky, J. L. Flares from small to large: X-ray spectroscopy of Proxima Centauri with XMM-Newton. *Astron. Astrophys.* **416**, 713–732 (2004).
- Kopparapu, R. K. *et al.* Habitable zones around main-sequence stars: new estimates. *Astrophys. J.* **765**, 131 (2013).
- Pepe, F. *et al.* The HARPS search for Earth-like planets in the habitable zone. I. Very low-mass planets around HD 20794, HD 85512, and HD 192310. *Astron. Astrophys.* **534**, A58 (2011).
- Anglada-Escudé, G. & Butler, R. P. The HARPS-TERRA Project. I: description of the algorithms, performance, and new measurements on a few remarkable stars observed by HARPS. *Astrophys. J. Suppl. Ser.* **200**, 15 (2012).
- Butler, R. P. *et al.* Attaining Doppler precision of 3 m s^{-1} . *Publ. Astron. Soc. Pacif.* **108**, 500–509 (1996).
- Kürster, M. *et al.* The low-level radial velocity variability in Barnard's star (= GJ 699): secular acceleration, indications for convective redshift, and planet mass limits. *Astron. Astrophys.* **403**, 1077–1087 (2003).
- Arriagada, P. *et al.* Two planetary companions around the K7 dwarf GJ 221: a hot super-Earth and a candidate in the sub-Saturn desert range. *Astrophys. J.* **771**, 42 (2013).
- Berdiñas, Z. M., Amado, P. J., Anglada-Escudé, G., Rodríguez-López, C. & Barnes, J. High-cadence spectroscopy of M-dwarfs. I: analysis of systematic effects in HARPS-N line profile measurements on the bright binary GJ 725A+B. *Mon. Not. R. Astron. Soc.* **459**, 3551B (2016).
- Sicardy, B. *et al.* A Pluto-like radius and a high albedo for the dwarf planet Eris from an occultation. *Nature* **478**, 493–496 (2011).
- Brown, T. M. *et al.* Las Cumbres Observatory Global Telescope Network. *Publ. Astron. Soc. Pacific* **125**, 1031–1055 (2013).
- Baluev, R. V. The impact of red noise in radial velocity planet searches: only three planets orbiting GJ 581? *Mon. Not. R. Astron. Soc.* **429**, 2052–2068 (2013).
- Tuomi, M., Jones, H. R. A., Barnes, J. R., Anglada-Escudé, G. & Jenkins, J. S. Bayesian search for low-mass planets around nearby M dwarfs—estimates for occurrence rate based on global detectability statistics. *Mon. Not. R. Astron. Soc.* **441**, 1545–1569 (2014).
- Haario, H., Laine, M., Mira, A. & Saksman, E. Dram: efficient adaptive MCMC. *Stat. Comput.* **16**, 339–354 (2006).
- Rajpaul, V., Aigrain, S. & Roberts, S. Ghost in the time series: no planet for Alpha Cen B. *Mon. Not. R. Astron. Soc.* **456**, L6–L10 (2016).
- Bonfils, X. *et al.* The HARPS search for southern extra-solar planets. X: A $m_{\text{Jup}} = 11 M_{\text{Jup}}$ planet around the nearby spotted M dwarf GJ 674. *Astron. Astrophys.* **474**, 293–299 (2007).
- Barnes, J. R. *et al.* Precision radial velocities of 15 M5–M9 dwarfs. *Mon. Not. R. Astron. Soc.* **439**, 3094–3113 (2014).
- Ofir, A. Optimizing the search for transiting planets in long time series. *Astron. Astrophys.* **561**, A138 (2014).
- Kopparapu, R. K. *et al.* The inner edge of the habitable zone for synchronously rotating planets around low-mass stars using general circulation models. *Astrophys. J.* **819**, 84 (2016).
- Reiners, A. & Basri, G. The moderate magnetic field of the flare star Proxima Centauri. *Astron. Astrophys.* **489**, L45–L48 (2008).
- Vidotto, A. A. *et al.* Effects of M dwarf magnetic fields on potentially habitable planets. *Astron. Astrophys.* **557**, A67 (2013).
- Zuluaga, J. I., Bustamante, S., Cuartas, P. A. & Hoyos, J. H. The influence of thermal evolution in the magnetic protection of terrestrial planets. *Astrophys. J.* **770**, 23 (2013).
- Bolmont, E. *et al.* Water loss from Earth-sized planets in the habitable zones of ultracool dwarfs: implications for the planets of TRAPPIST-1. Preprint at <http://arxiv.org/abs/1605.00616> (2016).
- Tanaka, H., Takeuchi, T. & Ward, W. R. Three-dimensional interaction between a planet and an isothermal gaseous disk. I: corotation and Lindblad torques and planet migration. *Astrophys. J.* **565**, 1257–1274 (2002).
- Weidenschilling, S. J. Aerodynamics of solid bodies in the solar nebula. *Mon. Not. R. Astron. Soc.* **180**, 57–70 (1977).
- Snellen, I. *et al.* Combining high-dispersion spectroscopy with high contrast imaging: probing rocky planets around our nearest neighbors. *Astron. Astrophys.* **576**, A59 (2015).
- Lubin, P. A roadmap to interstellar flight. Preprint at <http://arxiv.org/abs/1604.01356> (2016).
- Delfosse, X. *et al.* Accurate masses of very low mass stars. IV. Improved mass-luminosity relations. *Astron. Astrophys.* **364**, 217–224 (2000).

Supplementary Information is available in the online version of the paper.

Acknowledgements We thank E. Gerlach, R. Street and U. Seemann for their support to the science preparations. We thank P. Micakovic, M. M. Mutter (QMUL), R. Ivison, G. Hussain, I. Saviane, O. Sandu, L. L. Christensen, R. Hook and the personnel at La Silla (ESO) for making the PRD campaign possible. The authors acknowledge support from the following funding grants: Leverhulme Trust/UK RPG-2014-281 (H.R.A.J., G.A.-E. and M.T.); MINECO/Spain AYA-2014-54348-C3-1-R (P.J.A., C.R.-L., Z.M.B. and E.R.); MINECO/Spain ESP2014-54362-P (M.J.L.-G.); MINECO/Spain AYA-2014-56637-C2-1-P (J.L.O. and N.M.); J.A./Spain 2012-FQM1776 (J.L.O. and N.M.); CATA-Basal/Chile PB06 Conicyt (J.S.J.); Fondecyt/Chile project #1161218 (J.S.J.); STFC/UK ST/M001008/1 (R.P.N., G.A.L.C. and G.A.-E.); STFC/UK ST/L000776/1 (J.B.); ERC/EU Starting Grant #279347 (A.R., L.F.S. and S.V.J.); DFG/Germany Research Grants RE 1664/9-2 (A.R.); RE 1664/12-1 (M.Z.); DFG/Germany Collaborative Research Center 963 (C.J.M. and S.D.); DFG/Germany Research Training Group 1351 (L.F.S.); and NSF/USA grant AST-1313075 (M.E.). Study based on observations made with ESO Telescopes at the La Silla Paranal Observatory under programmes 096.C-0082 and 191.C-0505. Observations were obtained with ASH2, which is supported by the Instituto de Astrofísica de Andalucía and Astroimagen. This work makes use of observations from the LCOGT network. We acknowledge the effort of the UVES/M-dwarf and the HARPS/Geneva teams, who obtained a substantial amount of the data used in this work.

Author Contributions In the author list, after G.A.-E., the authors are listed in alphabetical order. G.A.-E. led the PRD campaign, observing proposals and organized the manuscript. P.J.A. led observing proposals and organized and supported the Instituto de Astrofísica de Andalucía team through research grants. M.T. obtained the early signal detections and most of the Bayesian analyses. J.S.J., J.B., Z.M.B. and H.R.A.J. participated in the analyses and obtained activity measurements. Z.M.B. also led observing proposals. H.R.A.J. funded several co-authors via research grants. M. Kuerster and M.E. provided the extracted UVES spectra, and R.P.B. re-derived radial velocity measurements. C.R.-L. coordinated photometric follow-up campaigns. E.R. led the ASH2 team and related reductions (M.J.L.-G., I.d.L.C., J.L.O. and N.M.). Y.T. led the LCOGT proposals, campaign and reductions. M.Z. obtained observations and performed analyses on HARPS and UVES spectra. A.O. analysed time series and transit searches. J.M., S.V.J. and A.R. analysed stellar activity data. A.R. funded several co-authors via research grants. R.P.N., G.A.L.C., S.-J.P., S.D. and B.G. did dynamical studies and studied the planet formation context. M. Kiraga provided early access to time series from the ASAS survey. C.J.M. and L.F.S. participated in the HARPS campaigns. All authors contributed to the preparation of observing proposals and the manuscript.

Author Information Reprints and permissions information is available at www.nature.com/reprints. The authors declare no competing financial interests. Readers are welcome to comment on the online version of the paper. Correspondence and requests for materials should be addressed to G.A.-E. (g.anglada@qmul.ac.uk).

Reviewer Information *Nature* thanks A. Hatzes and D. Queloz for their contribution to the peer review of this work.

METHODS

Statistical frameworks and tools. The analyses of time series including the radial velocities and activity indices were performed by frequentist and Bayesian methods. In all cases, the statistical significance was assessed using model comparisons by performing global multiparametric fits to the data. Here we provide a minimal overview of the methods and assumptions used throughout the Letter.

Bayesian statistical analyses. The analyses of the radial velocity data were performed by applying posterior sampling algorithms called Markov chain Monte Carlo methods. We used the adaptive Metropolis algorithm³¹, which has previously been applied to such radial velocity data sets^{15,32}. This algorithm is simply a generalized version of the common Metropolis–Hastings algorithm^{33,34} that adapts to the posterior density based on the previous members of the chain.

The likelihood functions and posterior densities of models with periodic signals are highly multimodal (that is, they have peaks in the periodograms). For this reason, in our Bayesian signal searches we applied the delayed rejection adaptive Metropolis (DRAM) method¹⁶, which enables efficient jumping of the chain between multiple modes by postponing the rejection of a proposed parameter vector by first attempting to find a better value in its vicinity. For every given model we performed several posterior samplings with different initial values to ensure convergence to a unique solution. When we identified two or more substantial maxima in the posterior density, we typically performed several additional samplings with initial states close to those maxima. This enabled us to evaluate their relative importance in a consistent manner. We estimated the marginal likelihoods and the corresponding Bayesian evidence ratios of different models by using a simple method³⁵. A more detailed description of these methods can be found in elsewhere³⁶.

Doppler model and likelihood function. Assuming that the i th radial velocity measurements is $m_{i,INS}$ obtained at some instant t_i from an instrument INS, the likelihood function of the observations (probability of the data given a model) is given by

$$L = \prod_{INS} \prod_i I_{i,INS} \quad (1)$$

$$I_{i,INS} = \frac{1}{\sqrt{2\pi(\sigma_i^2 + \sigma_{INS}^2)}} \exp\left[-\frac{1}{2} \frac{\epsilon_{i,INS}^2}{\sigma_i^2 + \sigma_{INS}^2}\right] \quad (2)$$

$$\epsilon_{i,INS} = m_{i,INS} - \{\gamma_{INS} + \dot{\gamma}\Delta t_i + \kappa(\Delta t_i) + MA_{i,INS} + A_{i,INS}\} \quad (3)$$

$$\Delta t_i = t_i - t_0 \quad (4)$$

where t_0 is some reference epoch. This reference epoch can be arbitrarily chosen, often as the beginning of the time series or a mid-point of the observing campaigns. The other terms are:

(1) $\epsilon_{i,INS}$ are the residuals to a fit. We assume that each $\epsilon_{i,INS}$ value is a Gaussian random variable with a zero mean and a variance of $\sigma_i^2 + \sigma_{INS}^2$, where σ_i^2 is the reported uncertainty of the i th measurement and is the jitter parameter and σ_{INS}^2 represents the excess white noise not included in σ_i^2 .

(2) γ_{INS} is the zero-point velocity of each instrument. Each INS can have a different zero point depending on how the radial velocities are measured and how the wavelengths are calibrated.

(3) $\dot{\gamma}$ is a linear trend parameter caused by a long-term acceleration.

(4) The term $\kappa(\Delta t_i)$ is the superposition of k Keplerian signals evaluated at Δt_i . Each k depends on five parameters: the orbital period P_p , the semi-amplitude of the signal K_p , the mean anomaly $M_{0,p}$, which represents the phase of the orbit with respect to the periastron of the orbit at t_0 , the orbital eccentricity e_p that goes from 0 (circular orbit) to 1 (unbound parabolic orbit) and the argument of periastron ω_p , which is the angle on the orbital plane with respect to the plane of the sky at which the star goes through the periastron of its orbit (the planet's periastron is at $\omega_p + 180^\circ$). Detailed definitions of the parameters can be found elsewhere³⁷.

(5) The moving average term

$$MA_{i,INS} = \phi_{INS} \exp\left[-\frac{t_i - t_{i-1}}{\tau_{INS}}\right] \epsilon_{i-1,INS} \quad (5)$$

is a simple parameterization of the possible correlated noise that depends on the residual of the previous measurement $\epsilon_{i-1,INS}$. As for the other parameters related to noise in our model, we assume that the parameters of the MA function depend on the instrument; for example the different wavelength ranges used will cause different properties of the instrumental systematic noise. Keplerian and other physical processes also introduce correlations into the data, therefore some degree of degeneracy between the MA terms and the signals of interest is expected.

As a result, including an MA term always produces more conservative statistical significance estimates than a model with uncorrelated random noise only. The MA model is implemented through a coefficient ϕ_{INS} and a timescale τ_{INS} . ϕ_{INS} quantifies the strength of the correlation between the i and $i - 1$ measurements. It is bound between -1 and 1 to guarantee that the process is stationary (that is, the contribution of the MA term does not arbitrarily grow over time). Exponential smoothing is used to decrease the strength of the correlation exponentially as the difference $t_i - t_{i-1}$ increases³⁸.

(6) Linear correlations with activity indices can also be included in the model in the following manner

$$A_{i,INS} = \sum_{\xi} C_{\xi,INS} \xi_{i,INS} \quad (6)$$

where ξ runs over all of the activity indices used to model each INS data set (for example, m_2 , m_3 , S-index and so on, whose descriptions are provided below). To avoid any confusion with other discussions about correlations, we call these $C_{\xi,INS}$ activity coefficients. Note that each activity coefficient $C_{\xi,INS}$ is associated with one activity index (ξ_i) obtained simultaneously with the i th radial velocity measurement (for example, chromospheric emission from the H α line, the second moment of the mean-line profile, the interpolated photometric flux and so on). When fitting a model to the data, an activity coefficient substantially different from 0 indicates evidence of Doppler variability correlated with the corresponding activity index. Formally speaking, these $C_{\xi,INS}$ correspond to the coefficient of the first-order Taylor expansion of a physical model for the apparent radial velocities as a function of the activity indices and other physical properties of the star.

A simplified version of the same likelihood model is used when analysing time series of activity indices. That is, when searching for periodicities in series other than Doppler measurements, the model will consist of the γ_{INS} zero points, a linear trend term $\dot{\gamma}\Delta t_i$ and a sum of n sinusoids

$$\hat{\kappa}(t_i, \theta) = \sum_k^n \left(A_k \sin \frac{2\pi\Delta t_i}{P_k} + B_k \cos \frac{2\pi\Delta t_i}{P_k} \right) \quad (7)$$

where each k th sinusoid has three parameters A_k , B_k and P_k instead of the five Keplerian ones. Except for the period parameters and the jitter terms, this model is linear with all the other parameters, which allows a relatively quick computation of the likelihood-ratio periodograms.

Bayesian prior choices. As in any Bayesian analysis, the prior densities of the model parameters have to be selected in a suitable manner (for example see ref. 39). We used uniform and uninformative distributions for most of the parameters apart from a few, possibly important, exceptions. First, as we used a parameter $l = \ln P$ in the Markov chain Monte Carlo samplings instead of the period P directly, the uniform prior density $\pi(l) = c$ for all $l \in [\ln P_0, \ln P_{\max}]$, where P_0 and P_{\max} are some minimum and maximum periods, does not correspond to a uniform prior in P . Instead, this prior corresponds to a period prior such that $\pi(P) \propto P^{-1}$ (ref. 40). We made this choice because the period can be considered a scale parameter for which an uninformative prior is one that is uniform in $\ln P$ (ref. 41). We selected the parameter space of the period such that $P_0 = 1$ d and $P_{\max} = T_{\text{obs}}$, where T_{obs} is the time baseline of the combined data sets.

For the semi-amplitude parameter K , we used a $\pi(K) = c$ for all $K \in [0, K_{\max}]$, where K_{\max} was selected as 10 m s^{-1} because the r.m.s. of the Doppler series did not exceed 3 m s^{-1} in any of the sets. Following previous works^{40,42}, we chose the prior for the orbital eccentricities as $\pi(e) \propto \mathcal{N}(0, \Sigma_e^2)$, where e is bound between zero (circular orbit) and 1. We set this $\Sigma_e^2 = 0.3$ to penalize high eccentricities while keeping the option of high e if the data strongly favours it.

We also used an informative prior for the excess white noise parameter of σ_{INS} for each instrument. Based on analyses of a sample of M dwarfs¹⁵, this stellar jitter is typically very close to a value of 1 m s^{-1} . Thus, we used a prior such that $\pi(\sigma) \propto \mathcal{N}(\mu_\sigma, \sigma_\sigma^2)$ the parameters were selected as $\mu_\sigma = \sigma_\sigma = 1 \text{ m s}^{-1}$. Uniform priors were used in all the activity coefficients $C_\xi \in [-C_{\xi,\max}, C_{\xi,\max}]$. For practical purposes, the time series of all activity indices were mean subtracted and normalized to their r.m.s. This choice allows us to select the bounds of the activity coefficients for the renormalized time series as $\hat{C}_{\xi,\max} = 3 \text{ m s}^{-1}$, so that adding correlation terms does not dramatically increase the r.m.s. of the Doppler time series over the initially measured r.m.s. of $< 3 \text{ m s}^{-1}$ (same argument as for the prior on K). This renormalization is automatically applied by our codes at initialization. **Search for periodicities and statistically significant signals in a frequentist framework.** Periodograms are plots that represent a figure of merit derived from a fit against the period of a newly proposed signal. In the case of unevenly sampled data, a very popular periodogram is the Lomb–Scargle periodogram^{43,44} and its variants, such as the Floating-mean periodogram⁴⁵ or the F-ratio periodogram⁴⁶. In this work we use likelihood ratio periodograms, which represent the improvement of

the likelihood statistic when adding a new sinusoidal signal to the model. Owing to intrinsic nonlinearities in the Keplerian/radial velocity modelling, optimizing the likelihood statistic is more computationally intensive than the classic Lomb–Scargle-like periodograms^{45,47}. On the other hand, the likelihood function is a more general and well behaved statistic that, for example, allows for the optimization of the noise parameters (such as jitter and the fit correlated noise models at the signal search level). By well-behaved we mean that it has less intrinsic variance compared with other statistics that do not include parameters for the noise such as the χ^2 statistic. Once the maximum likelihood of a model with one additional planet is found (the highest peak in the periodogram), its FAP can then be easily computed^{14,48}. In general, an FAP of 1% is needed to claim hints of variability, and a value below 0.1% is considered necessary to claim a statistically significant detection.

Spectroscopic data sets. *New reduction of the UVES M-dwarf programme data.* Between 2000 and 2008, Proxima was observed in the framework of a precision radial velocity survey of M dwarfs in search for extrasolar planets with UVES installed in the Very Large Telescope unit 2. To attain high-precision radial velocity measurements, UVES was self-calibrated with its iodine gas absorption cell operated at a temperature of 70 °C. Image slicer number 3 was chosen, which redistributes the light from a $1'' \times 1''$ aperture along the chosen 0.3''-wide slit. In this way, a resolving power of $R = 100,000\text{--}120,000$ was attained. At the selected central wavelength of 600 nm, the useful spectral range containing iodine (I_2) absorption lines (500–600 nm) falls entirely on the better-quality detector of the mosaic of two $4K \times 2K$ CCDs. More details can be found in the several papers from the UVES survey^{9,45,49}.

The extracted UVES spectra include 241 observations taken through the iodine cell, three template (no iodine) shots of Proxima and three spectra of the rapidly rotating B star HR 5987 that are also taken through the iodine cell and almost consecutive to the three template shots. The B star has a smooth spectrum devoid of spectral features and it was used to calibrate the three template observations of the target. Ten of the iodine observations of Proxima were eliminated due to low exposure levels. The remaining 231 iodine shots of Proxima were taken on 77 nights, typically 3 consecutive shots per night.

The first steps in the processing of the I_2 -calibrated data consists of constructing the high signal-to-noise template spectrum of the star without iodine: (1) a custom model of the UVES instrumental profile is generated on the basis of the observations of the B star by forward modelling the observations using a higher-resolution ($R = 700,000\text{--}1,000,000$) template spectrum of the I_2 cell obtained with the McMath Fourier Transform Spectrometer (FTS) on Kitt Peak; (2) the three template observations of Proxima are then co-added and filtered for outliers; and (3) on the basis of the instrument profile model and wavelength solution derived from the three B star observations, the template is deconvolved with our standard software¹⁰. After the creation of the stellar template, the 231 iodine observations of Proxima were then run through our standard precision velocity code⁸. The resulting standard deviation of the 231 unbinned observations is 2.58 m s^{-1} , and the standard deviation of the 77 nightly binned observations is 2.30 m s^{-1} , which already suggests an improvement compared to the 3.11 m s^{-1} reported in the original UVES survey reports⁴⁹. All of the UVES spectra (raw) are publicly available in their reduced form via the ESO's archive at <http://archive.eso.org/cms.html>. Extracted spectra are not produced for this mode of UVES operation, but they are available upon request from the corresponding author.

HARPS GTO. The initial HARPS-Guaranteed Time Observations programme was led by M. Mayor (ESO ID: 072.C-0488). 19 spectra were obtained between May 2005 and July 2008. The typical integration time ranges between 450 s and 900 s.

HARPS M-dwarfs. Led by X. Bonfils and collaborators, this programme consists of ESO programmes 082.C-0718 and 183.C-0437. It produced 8 and 46 measurements, respectively, with integration times of 900 s in almost all cases⁵⁰.

HARPS high-cadence. This programme consisted of two 10-night runs (May 2013, and December 2013, ESO ID: 191.C-0505) and was led and executed by several co-authors of this work. Proxima was observed on two runs:

- (1) May 2013: 143 spectra obtained on three consecutive nights between 4 May and 7 May and 25 additional spectra between 7 May and 16 May with exposure times of 900 s.
- (2) December 2013: 23 spectra obtained between 30 December and 10 January 2014 also with 900 s exposure times.

For simplicity in the presentation of the data and analyses, all HARPS data obtained before 2016 (HARPS GTO, HARPS M-dwarfs, and HARPS high-cadence) are integrated in the HARPS pre-2016 set. The long-term Doppler variability and sparse sampling makes the detection of the Doppler signal more challenging in such a consolidated set than, for example, separating it into subsets of contiguous nights. The latter strategy, however, necessarily requires more parameters (offsets, jitter terms, correlated noise parameters) and arbitrary choices on the sets to be used, producing strong degeneracies and aliasing ambiguities in the determination of the favoured solution (11.2 d was typically favoured, but alternative periods caused by a non-trivial window function at 13.6 d and 18.3 d were also found

be possible). The data taken in 2016 exclusively correspond to the new campaign specifically designed to address the sampling issues.

HARPS PRD campaign. The PRD campaign was executed between 18 January and 30 March 2016. Interruptions of a few nights were anticipated to allow for technical work and other time-critical observations with HARPS. Of the 60 scheduled epochs, we obtained 56 spectra for 54 nights (two spectra were obtained on two of those nights). Integration times were set to 1,200 s, and observations were always obtained at the very end of each night. All of the HARPS spectra (raw, extracted and calibrated frames) are publicly available in their reduced form via ESO's archive at <http://archive.eso.org/cms.html>.

Spectroscopic indices. Stellar activity can be traced by features in the stellar spectrum. For example, changes in the line-profile shapes (symmetry and width) have been associated with spurious Doppler shifts^{18,51}. Chromospheric emission lines are tracers of spurious Doppler variability in the Sun and they are expected to behave similarly for other stars⁵². We describe here the indices measured and used in our analyses.

Measurements of the mean spectral line profiles. The HARPS Data Reduction Software provides two measurements of the mean-line profile shapes derived from the cross-correlation function (CCF) of the stellar spectrum with a binary mask. These are called the bisector span (or BIS) and full-width-at-half-maximum (or FWHM) of the CCF⁵⁰. For very-late-type stars like Proxima, all of the spectral lines are blended, producing a non-trivial shape of the CCF and thus the interpretation of the usual line-shape measurements is not nearly as reliable as in earlier-type stars. We applied the least-squares deconvolution (LSD) technique⁵³ to obtain a more accurate estimate of the spectral mean line profile. This profile is generated from the convolution of a kernel, which is a model spectrum of line positions and intensities, with the observed spectrum. A description of our implementation of the procedure, applied specifically to crowded M dwarf spectra is described in ref. 54. The LSD profile can be interpreted as a probability function distribution that can then be characterized by its central moments⁵⁵. We computed the second (m_2) and third (m_3) central moments of each LSD profile for each observation. More details of these indices and how they compare with other standard HARPS cross-correlation measurements can be found in ref. 11. To eliminate the correlation of the profile moments with the slope of the spectral energy distribution¹¹, we corrected the spectral energy distribution and blaze function to match the same spectral energy distribution of the highest signal-to-noise ratio (or S/N) observation obtained with HARPS. Uncertainties were obtained using an empirical procedure as follows: we derived all the m_2 and m_3 measurements of the high-cadence night of 7 May 2013 and fitted a polynomial to each time series. The standard deviation of the residuals to that fit was then assumed to be the expected uncertainty for a $S/N \approx 20$ (at reference echelle aperture number 60), which was the typical value for that night's observations. All other errors were then obtained by scaling this standard deviation by a factor of $\frac{20}{S/N_{\text{obs}}}$ for each observation.

Chromospheric indices. Chromospheric emission lines are tracers of spurious Doppler variability in the Sun and they are expected to behave similarly for other stars⁵². We describe here the indices computed and used in our analyses.

Chromospheric Ca II H+K S-index. We calculated the Ca II H+K fluxes following standard procedures^{56,57}, both the PRD data and the pre-2016 data were treated the same. Uncertainties were calculated from the quadrature sum of the variance in the data used within each bandpass.

Chromospheric H α emission. This index was measured in a similar way to the S-indices, in that we summed the fluxes in the centre of the lines, calculated to be 6,562.808 Å, this time using square bandpasses of 0.678 Å not triangular shapes, and those were normalized to the summed fluxes of two square continuum band regions surrounding each of the lines in the time series. The continuum square bandpasses were centred at 6,550.870 Å and 6,580.309 Å and had widths of 10.75 Å and 8.75 Å, respectively. Again the uncertainties were calculated from the quadrature sum of the variance of the data within the bandpasses.

Photometric data sets. **ASH2.** The ASH2 telescope is a 40 cm robotic telescope with a CCD camera STL11000 $2.7K \times 4K$, and a field-of-view (FOV) of 54×82 arcmin. Observations were obtained in two narrow-band filters centred on the H α and S II lines, respectively (H α is centred on 656 nm, S II is centred on 672 nm, and both filters have a Gaussian-like transmission with a FWHM of 12 nm). The telescope is at SPACEOBS (San Pedro de Atacama Celestial Explorations Observatory), at 2,450 m above sea level, located in the northern Atacama Desert in Chile. This telescope is managed and supported by the Instituto de Astrofísica de Andalucía (Spain). During the present work, only subframes with 40% of the total FOV were used, resulting in a useful FOV of 21.6×32.8 arcmin. Approximately 20 images in each band of 100 s of exposure time were obtained per night. In total, 66 epochs of about 100 min each were obtained during this campaign. The number of images collected per night was increased during the second part of the campaign (to about 40 images in each filter per night).

All CCD measurements were obtained by the method of synthetic aperture photometry using a 2×2 binning. Each CCD frame was corrected in a standard way for dark and flat-fielding. Different aperture sizes were also tested to choose the best one for our observations. A number of nearby and relatively bright stars within the frames were selected as check stars to choose the best ones to be used as comparison stars. After checking their stability, C2 = HD 126625 and C8 = TYC 9010-3029-1, were selected as main comparison stars.

The basic photometric data were computed as the differences in magnitude of the S II and H α filters for Var-X and C2-X, with Var = Proxima and X = C2 + C8)/2. Typical uncertainties of each individual data point are about 6.0 mmag, for both S II and H α filters. This usually leads to error bars of about 1.3 mmag in the determination of the mean levels of each epoch, assuming 20 points per night once occasional strong activity episodes (such as flares) are removed for the analysis of periodicities. For the analyses, these magnitudes were transformed to relative flux measurements normalized to the mean flux over the campaign.

LCOGT network. The LCOGT is an organization dedicated to time-domain astronomy¹³. To facilitate this, LCOGT operates a homogeneous network of 1 m and 2 m telescopes on multiple sites around the world. The telescopes are controlled by a single robotic scheduler, which is capable of orchestrating complex responsive observing programmes, using the entire network to provide uninterrupted observations of any astronomical target of interest. Each site hosts between one and three telescopes, which are configured for imaging and spectroscopy. The telescopes are equipped with identical instruments and filters, which allows for network redundancy. This means that observations can be seamlessly shifted to alternate sites at any time if the scientific programme requires it, or in the event of poor weather.

Observations for the PRD campaign were obtained on the 1 m network every 24 h in the B and V bands with the Sinistro ($4\text{K} \times 4\text{K}$ Fairchild CCD486) cameras, which have a pixel scale of 0.38 arcsec and a FOV of 27×27 arcminutes. In addition, B and V observations were taken every 12 h with the SBIG ($4\text{K} \times 4\text{K}$ Kodak KAF-6303E CCD) cameras, with a pixel scale of 0.46 arcsec and a FOV of 16×16 arcminutes. Exposure times ranged between 15 and 40 s and a total of 488 photometrically useful images were obtained during the campaign.

The photometric measurements were performed using aperture photometry with AstroImageJ⁵⁸ and DEFOT⁵⁹. The aperture sizes were optimized during the analysis with the aim of minimizing the measurement noise. Proxima and two non-variable comparison stars were identified in a reference image and used to construct the detrended light curves. As with the ASH2 curves, the LCOGT differential magnitudes were transformed to normalized flux to facilitate interpretation and later analyses (see Fig. 3).

Signals in time series. In this section we present a homogeneous analysis of all of the time series (Doppler, activity and photometric) presented in this Letter. In all of the periodograms, the black curve represents the search for a first signal. If one first signal is identified, then a red curve represents the search for a second signal. In the few cases where a second signal is detected, a blue curve represents the search for a third signal. The period of Proxima b is marked with a green vertical line.

Module of the window function. We first present the so-called window function of the three sets under discussion. The window function is the Fourier transform of the sampling⁶⁰. Its module shows the frequencies (or periods) where a signal with 0 frequency (or infinite period) would have its aliases. As shown in Extended Data Fig. 1, both the UVES and HARPS PRD campaigns have a relatively clear window function between 1 and 360 d, meaning that the peaks in periodograms can be interpreted in a very straightforward way (no aliasing ambiguities). For the UVES case, this happens because the measurements were uniformly spread over several years without severe clustering, producing only strong aliases at frequencies beating caused by the usual daily and yearly sampling (peaks at 360, 1, 0.5 and 0.33 d). The window of the PRD campaign is simpler, which is the result of a shorter time span and the uniform sampling of the campaign. On the other hand, the HARPS pre-2016 window function (Extended Data Fig. 1b) contains numerous peaks between 1 and 360 d. This means that signals (for example, activity) in the range of a few hundred days will inject severe interference in the period domain of interest, and explains why this set is where the Doppler signal at 11.2 d is detected with a lower confidence (see Extended Data Fig. 2).

Radial velocities. Here we present likelihood-ratio periodogram searches for signals in the three Doppler time series separately (PRD, HARPS pre-2016 and UVES). They are analysed in the same way as the activity indices to enable direct visual comparison. They differ from the ones presented in the main Letter in the sense that they do not include MA terms and the signals are modelled as pure sinusoids to mirror the analysis of the other time series as close as possible. The resulting periodograms are shown in Extended Data Fig. 2. A signal at 11.2 d was close to detection using UVES data only. However, let us note that the signal was not clearly detectable using the Doppler measurements as provided by the UVES survey⁴⁵, and it only became obvious when new Doppler measurements were re-derived using up-to-date iodine codes (see Methods subsection 'New reduction of the UVES

M-dwarf programme data'). The signal is weaker in the HARPS pre-2016 data set, but it still appears as a possible second signal after modelling the longer-term variability with a Keplerian at 200 d. Subsets of the HARPS pre-2106 data taken on consecutive nights (for example, HARPS high-cadence runs) also show strong evidence of the same signal. However splitting the data into subsets adds substantial complexity to the analysis and the results become quite sensitive to subjective choices (how to split the data and how to weight each subset). The combination of UVES with all the HARPS pre-2016 (Fig. 1a) already produced an FAP of 1%, but a dedicated campaign was deemed necessary given the caveats with the sampling and activity related variability. The HARPS PRD campaign unambiguously identifies a signal with the same period of approximately 11.2 d. As discussed earlier, the combination of all the data results in a very high significance (FAP $< 10^{-7}$), which implies that the period, but also the amplitude and phase are consistent in all three sets.

Photometry signals and calculation of the FF' index. The nightly average of the four photometric series was computed after removing the measurements clearly contaminated by flares (see Fig. 3). This produces 43 LCOGT epochs in the B and V bands (80 nights), and 66 ASH2 epochs in both S II and H α bands (100 nights covered). The precision of each epoch was estimated using the internal dispersion within a given night. All four photometric series show evidence of a long-period signal that is compatible with a photometric cycle at 83 d (probably the rotation) reported before³. See periodograms in Extended Data Fig. 3.

In the presence of spots, it has been proposed that spurious variability should be linearly correlated with the value of the normalized flux of the star F , the derivative of the flux F' , and the product of FF' (ref. 61) in what is sometimes called the FF' model. To include the photometry in the analysis of the Doppler data, we used the best model fit of the highest-quality light curve (ASH2 S II, which has the lowest post-fit scatter) to estimate F , F' and FF' at the instant of each PRD observation. The relation of F , F' and FF' to the Doppler variability is investigated later in the Bayesian analysis of the correlations.

Width of the mean spectral line as measured by m_2 . The m_2 measurement contains a strong variability that closely mirrors the measurements from the photometric time series (see Fig. 3). As in the photometry, the rotation period and its first harmonic (approximately 40 d) are clearly detected in the PRD campaign (see Extended Data Fig. 4). This apparently good match needs to be verified on other stars as it might become a strong diagnostic for stellar activity in M stars. The analysis of the HARPS pre-2016 data also shows very strongly that m_2 is tracing the photometric rotation period of 83 d. The modelling of this HARPS pre-2016 requires a second sinusoid with $P_2 \approx 85$ d, which is peculiar given how close it is to P_1 . We suspect this is caused by photospheric features on the surface changing over time.

Asymmetry of the mean spectral lines as monitored by m_3 . The periodogram analysis of m_3 of the PRD run suggests a signal at 24 d, which is close to twice the Doppler signal of the planet candidate (see Extended Data Fig. 5). However, line asymmetries are expected to be directly correlated with Doppler signals, not at twice nor integer multiples of the Doppler period. In addition, the peak has an FAP of 5%, which makes it not significantly different from white noise. When looking at the HARPS pre-2016 data, strong beating is observed at 179 and 360 d, which is probably caused by a poorly sampled signal at that period or longer (possibly a magnetic cycle), or some residual systematic effect (possibly contamination by tellurics). In summary, m_3 does not show evidence of any stable signal in the range of interest.

Signal searches in the S-index. Although H α ⁵¹ and other lines such as the sodium doublet (NaD1 and NaD2)⁶² have been shown to be the best tracers for activity on M dwarfs, analysing the time series of the S-index is also useful because of its historical use in the long-term monitoring of main-sequence stars⁶³. In Extended Data Fig. 6 we show the likelihood ratio periodograms for the S-indices of the HARPS pre-2016 and PRD time series. As can be seen, no signals were found around the 11 d period of the radial velocity signal, however two peaks were found close the 1% FAP threshold with periods of approximately 170 and 340 d. To further test the reality of these possible signals, we performed a Lomb–Scargle periodogram analysis⁴⁴ of the combined PRD and pre-2016 HARPS data. This test resulted in the marginal recovery of both the 170 and 340 d peaks seen in the likelihood periodograms, with no emerging peaks around the proposed 11 d Doppler signal. The Lomb–Scargle tests revealed some weak evidence for a signal at much lower periods, around 7 and 30 d.

Given that there is evidence for substantial peaks close to periods of 1 yr, its first harmonic and the lunar period, we also analysed the window function of the time series to check if there was evidence that these peaks are artefacts from the combination of the window function pattern interfering with a real long-period activity signal in the data. The dominant power in the window function is found to increase at periods greater than 100 d, with a forest of strong peaks found in that domain, in comparison to that of sub-100 d periods, which is very flat, representing the noise floor of the time series. This indicates that there are likely to be strong interference patterns from the sampling in this region, and that the signal in the

radial velocity data are also not due to the sampling of the data. A similar study in the context of the HARPS M dwarf programme was also done on Proxima⁶². They compared several indices and finally decided to use the intensity of the chromospheric sodium doublet lines. They did not report any notable period at the time, but we suspect this was due to using fewer measurements and not removing the frequent flaring events from the series, which also requires the compilation of a number of observations to reliably identify the outliers caused by flares.

Signal searches in H α emission. Our likelihood-ratio periodograms for H α (Extended Data Fig. 7) only show non-significant peaks in the 30–40 d period range. It is important to note that the analyses described above have been performed on multiple versions of the data set, in the sense that we analysed the full data set without removing measurements affected by flaring, then proceeded to reanalyse the activities by dropping data clearly following the flaring periods that Proxima went through when we observed the star. This allowed us to better understand the impact that flares and outliers have on signal interference in the activity indices. Although the distribution of the peaks in periodograms changes somewhat depending on how stringent the cuts are, no emerging peaks were seen close to an 11 d period. Concerning UVES H α measurements, our likelihood-ratio periodogram did not detect any statistically significant signal.

Further tests on the signal. It has been shown⁶⁴ that at least some of the ultraprecise photometric time series measured by the CoRoT and Kepler space missions do not have a necessary property to be represented by a Fourier expansion: the underlying function, from which the observations are a sample, must be analytic. An algorithm introduced in ref. 64 can test this property and was applied to the PRD data. The result is that, contrary to the light curves aforementioned, claims that the underlying function is non-analytic does not hold with the information available. Although the null hypothesis cannot be definitively rejected, at least until more data are gathered, our results are consistent with the hypothesis that a harmonic component is present in the Doppler time series.

Flares and radial velocities. Among the high-cadence data from May 2013 with HARPS, two strong flares are fully recorded. During these events, all of the chromospheric lines become prominent in emission, H α being the one that best traces the characteristic time dependence of flares observed on other stars and the Sun. The spectrum and impact of flares on the radial velocities will be described elsewhere in detail. Relevant to this study, we show that the typical flares on Proxima do not produce correlated Doppler shifts (Extended Data Fig. 8). This justifies the removal of obvious flaring events when investigating signals and correlations in the activity indices.

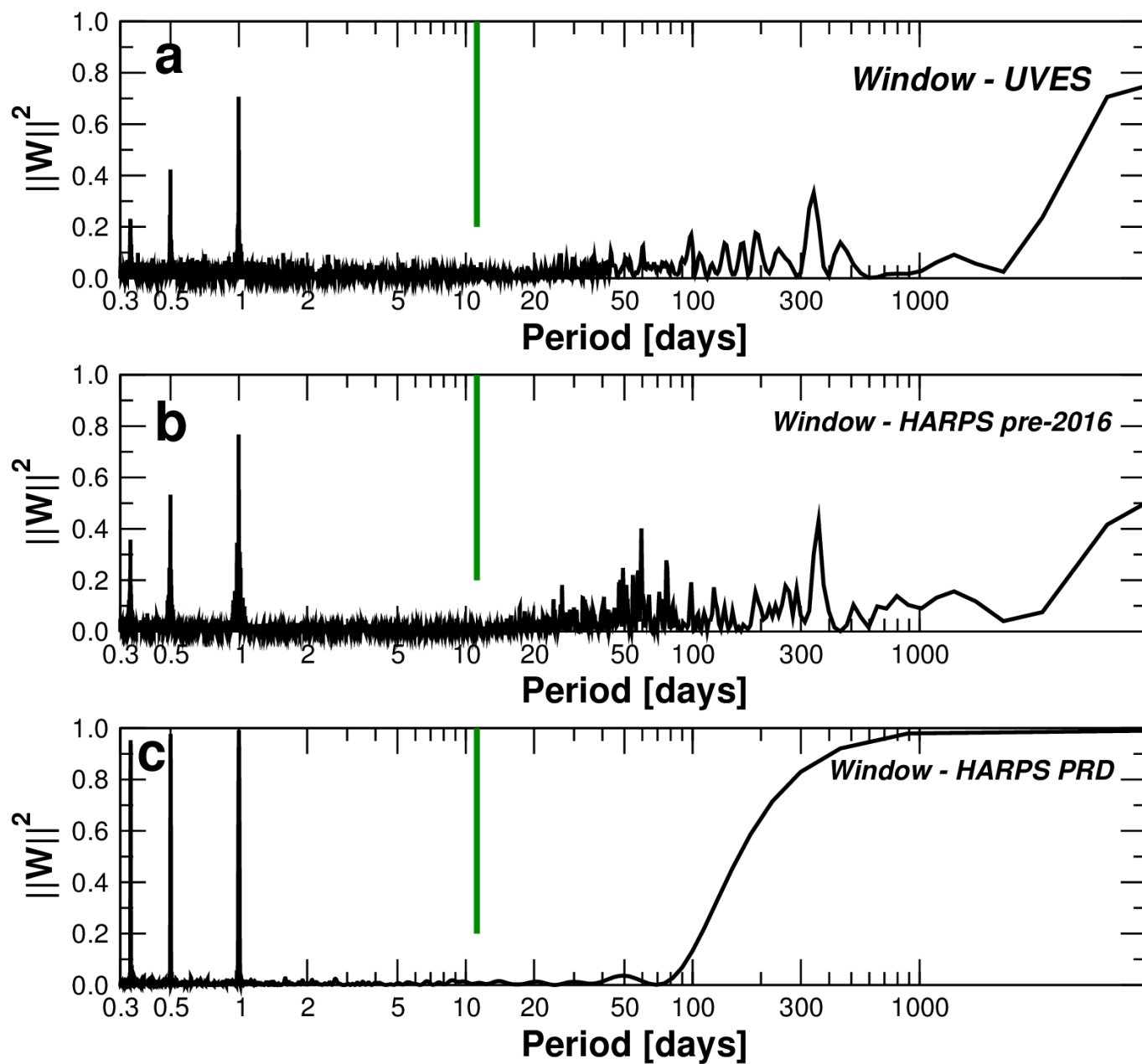
Complete model and Bayesian analysis of the activity coefficients. A global analysis including all of the radial velocities and indices was performed to verify that the inclusion of correlations would reduce the model probability below the detection thresholds. Equivalently, the Doppler semi-amplitude would become consistent with zero if the Doppler signal was to be described by a linear correlation term. Extended Data Fig. 9 shows the marginalized distributions of linear correlation coefficients with the Doppler semi-amplitude K . Each subset is treated as a separate instrument and has its own zero point, jitter and MA term (coefficient) and its own activity coefficients. In the final model, the timescales of the MA terms are fixed to around 10 d because they were not constrained within the prior bounds, thus compromising the convergence of the chains. The sets under consideration are: (1) UVES. 70 radial velocity measurements and corresponding H α emission measurements.

(2) HARPS pre-2016. 90 radial velocity measurements obtained between 2002 and 2014 by several programmes and corresponding spectroscopic indices: m_2 , m_3 , S-index and the intensities of the H α and He I lines as measured on each spectrum.

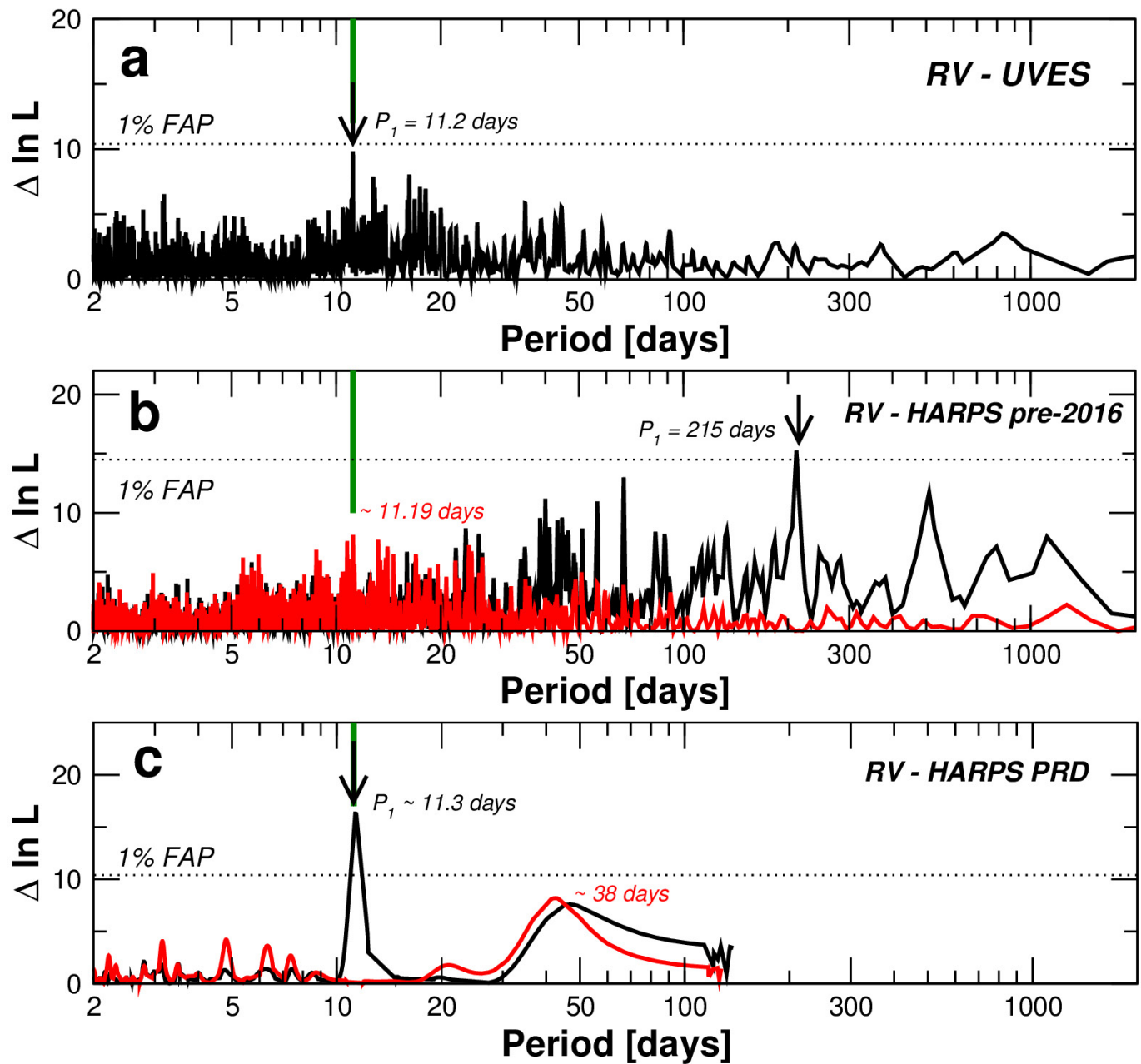
(3) HARPS PRD. 54 Doppler measurements obtained between 18 January–31 March 2016, and the same spectroscopic indices as for the HARPS pre-2016. The values of the F , F' and FF' indices were obtained by evaluating the best fit model to the ASH2 S II photometric series at the HARPS epochs (see Methods subsection 'Photometry signals and calculation of the FF' index').

An activity index is correlated with the radial velocity measurements in a given set if the zero value of its activity coefficient is excluded from the 99% credibility interval. Extended Data Fig. 9 shows the equiprobability contours that contain 50%, 95%, and 99% of the probability density around the mean estimate, and the corresponding 1σ uncertainties in red. Only the F' index (the time derivative of the photometric variability) is substantially different from 0 at high confidence (Extended Data Fig. 9m). Linking this correlation to a physical process requires further investigation. To ensure that such correlations are causally related, one needs a model of the process causing the signal in both the radial velocity and the index, and in the case of the photometry one would need to simultaneously cover more stellar photometric periods to verify that the relation holds over time. Extended Data Table 1 contains a summary of all of the free parameters in the model, including the activity coefficients for each data set.

31. Haario, H., Saksman, E. & Tamminen, J. An adaptive Metropolis algorithm. *Bernoulli* **7**, 223 (2001).
32. Tuomi, M. *et al.* Signals embedded in the radial velocity noise: periodic variations in the τ Ceti velocities. *Astron. Astrophys.* **551**, A79 (2013).
33. Metropolis, N., Rosenbluth, A., Rosenbluth, M., Teller, A. & Teller, E. Equations of state calculations by fast computing machines. *J. Chem. Phys.* **21**, 1087–1092 (1953).
34. Hastings, W. K. Monte Carlo sampling methods using Markov chains and their applications. *Biometrika* **57**, 97–109 (1970).
35. Newton, M. A. & Raftery, A. E. Approximate Bayesian inference with the weighted likelihood bootstrap. *J. R. Stat. Soc. B* **56**, 3–48 (1994).
36. Tuomi, M. A new cold sub-Saturnian candidate planet orbiting GJ 221. *Mon. Not. R. Astron. Soc.* **440**, L1–L5 (2014).
37. Wright, J. T. & Howard, A. W. Efficient fitting of multiplanet Keplerian models to radial velocity and astrometry data. *Astrophys. J. Suppl. Ser.* **182**, 205–215 (2009).
38. Scargle, J. D. Studies in astronomical time series analysis. I: modeling random processes in the time domain. *Astrophys. J. Suppl. Ser.* **45**, 1–71 (1981).
39. Tuomi, M. Evidence for nine planets in the HD 10180 system. *Astron. Astrophys.* **543**, A52 (2012).
40. Tuomi, M. & Anglada-Escudé, G. Up to four planets around the M dwarf GJ 163: sensitivity of Bayesian planet detection criteria to prior choice. *Astron. Astrophys.* **556**, A111 (2013).
41. Berger, J. O. *Statistical Decision Theory and Bayesian Analysis* Section 3.3 (Springer, 1980).
42. Anglada-Escudé, G. *et al.* A dynamically-packed planetary system around GJ 667C with three super-Earths in its habitable zone. *Astron. Astrophys.* **556**, A126 (2013).
43. Lomb, N. R. Least-squares frequency analysis of unequally spaced data. *Astrophys. Space Sci.* **39**, 447–462 (1976).
44. Scargle, J. D. Studies in astronomical time series analysis. II: statistical aspects of spectral analysis of unevenly spaced data. *Astrophys. J.* **263**, 835–853 (1982).
45. Zechmeister, M., Kürster, M. & Endl, M. The M dwarf planet search programme at the ESO VLT + UVES: a search for terrestrial planets in the habitable zone of M dwarfs. *Astron. Astrophys.* **505**, 859–871 (2009).
46. Cumming, A. Detectability of extrasolar planets in radial velocity surveys. *Mon. Not. R. Astron. Soc.* **354**, 1165–1176 (2004).
47. Ferraz-Mello, S. Estimation of periods from unequally spaced observations. *Astron. J.* **86**, 619–624 (1981).
48. Baluev, R. V. Accounting for velocity jitter in planet search surveys. *Mon. Not. R. Astron. Soc.* **393**, 969–978 (2009).
49. Endl, M. & Kürster, M. Toward detection of terrestrial planets in the habitable zone of our closest neighbor: Proxima Centauri. *Astron. Astrophys.* **488**, 1149–1153 (2008).
50. Bonfils, X. *et al.* The HARPS search for southern extra-solar planets. XXXI: the M-dwarf sample. *Astron. Astrophys.* **549**, A109 (2013).
51. Queloz, D. *et al.* No planet for HD 166435. *Astron. Astrophys.* **379**, 279–287 (2001).
52. Robertson, P., Mahadevan, S., Endl, M. & Roy, A. Stellar activity masquerading as planets in the habitable zone of the M dwarf Gliese 581. *Science* **345**, 440–444 (2014).
53. Donati, J.-F. & Brown, S. F. Zeeman–Doppler imaging of active stars. V: sensitivity of maximum entropy magnetic maps to field orientation. *Astron. Astrophys.* **326**, 1135–1142 (1997).
54. Barnes, J. R. *et al.* Red Optical Planet Survey: a new search for habitable Earths in the southern sky. *Mon. Not. R. Astron. Soc.* **424**, 591–604 (2012).
55. Press, W. H., Teukolsky, S. A., Vetterling, W. T. & Flannery, B. P. *Numerical Recipes in FORTRAN. The Art of Scientific Computing* 2nd edn, Section 4.1 (Cambridge Univ. Press, 1992).
56. Jenkins, J. S. *et al.* An activity catalogue of southern stars. *Mon. Not. R. Astron. Soc.* **372**, 163–173 (2006).
57. Jenkins, J. S. *et al.* Metallicities and activities of southern stars. *Astron. Astrophys.* **485**, 571–584 (2008).
58. Collins, K. A., Kielkopf, J. F. & Stassun, K. G. AstrolmageJ: image processing and photometric extraction for ultra-precise astronomical light curves. Preprint at <http://arxiv.org/abs/1601.02622> (2016).
59. Southworth, J. *et al.* High-precision photometry by telescope defocussing. VI: WASP-24, WASP-25 and WASP-26. *Mon. Not. R. Astron. Soc.* **444**, 776–789 (2014).
60. Dawson, R. I. & Fabrycky, D. C. Radial velocity planets de-aliased: a new, short period for super-Earth 55 Cnc e. *Astrophys. J.* **722**, 937–953 (2010).
61. Aigrain, S., Pont, F. & Zucker, S. A simple method to estimate radial velocity variations due to stellar activity using photometry. *Mon. Not. R. Astron. Soc.* **419**, 3147–3158 (2012).
62. Gomes da Silva, J. *et al.* Long-term magnetic activity of a sample of M-dwarf stars from the HARPS program. II: activity and radial velocity. *Astron. Astrophys.* **541**, A9 (2012).
63. Baliunas, S. L. *et al.* Chromospheric variations in main-sequence stars. *Astrophys. J.* **438**, 269–287 (1995).
64. Pascual-Granado, J., Garrido, R. & Suárez, J. C. Limits in the application of harmonic analysis to pulsating stars. *Astron. Astrophys.* **581**, A89 (2015).

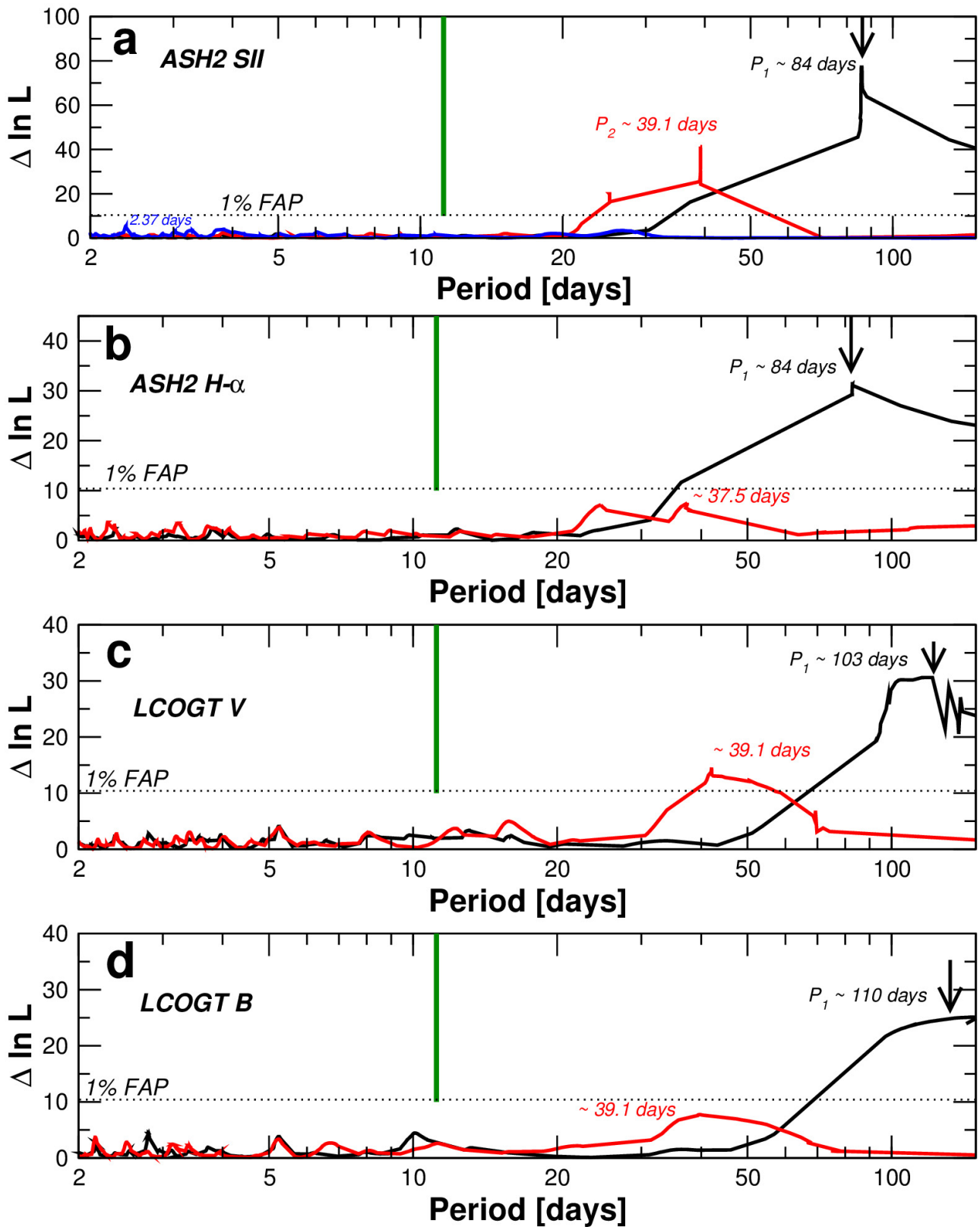


Extended Data Figure 1 | Window function. a–c, Window function of the UVES (a), HARPS pre-2016 (b) and HARPS PRD (c) data sets. The same window function applies to the time series of Doppler and activity data. Peaks in the window function are periods at which aliases of infinite period signals would be expected. The green vertical lines mark the period of the planet candidate at 11.2 d.



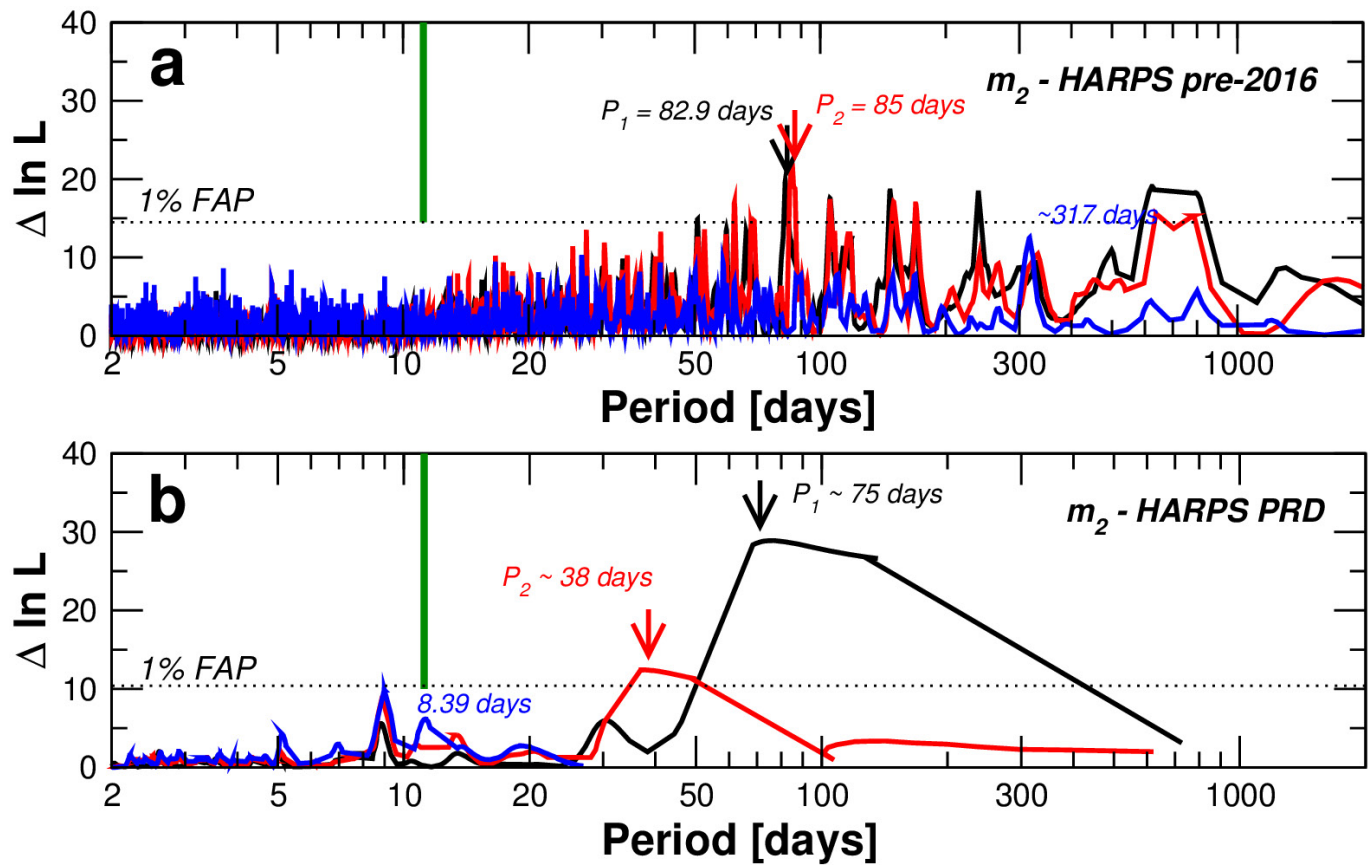
Extended Data Figure 2 | Signal searches on independent radial velocity data sets. a–c, Likelihood-ratio periodograms searches on the radial velocity (RV) measurements of the UVES (a), HARPS pre-2016 (b) and HARPS PRD (c) subsets. The periodogram with all three sets combined is

shown in Fig. 1. The black and red lines represent the searches for the first and second signals, respectively. The green vertical lines mark the period of the planet candidate at 11.2 d.



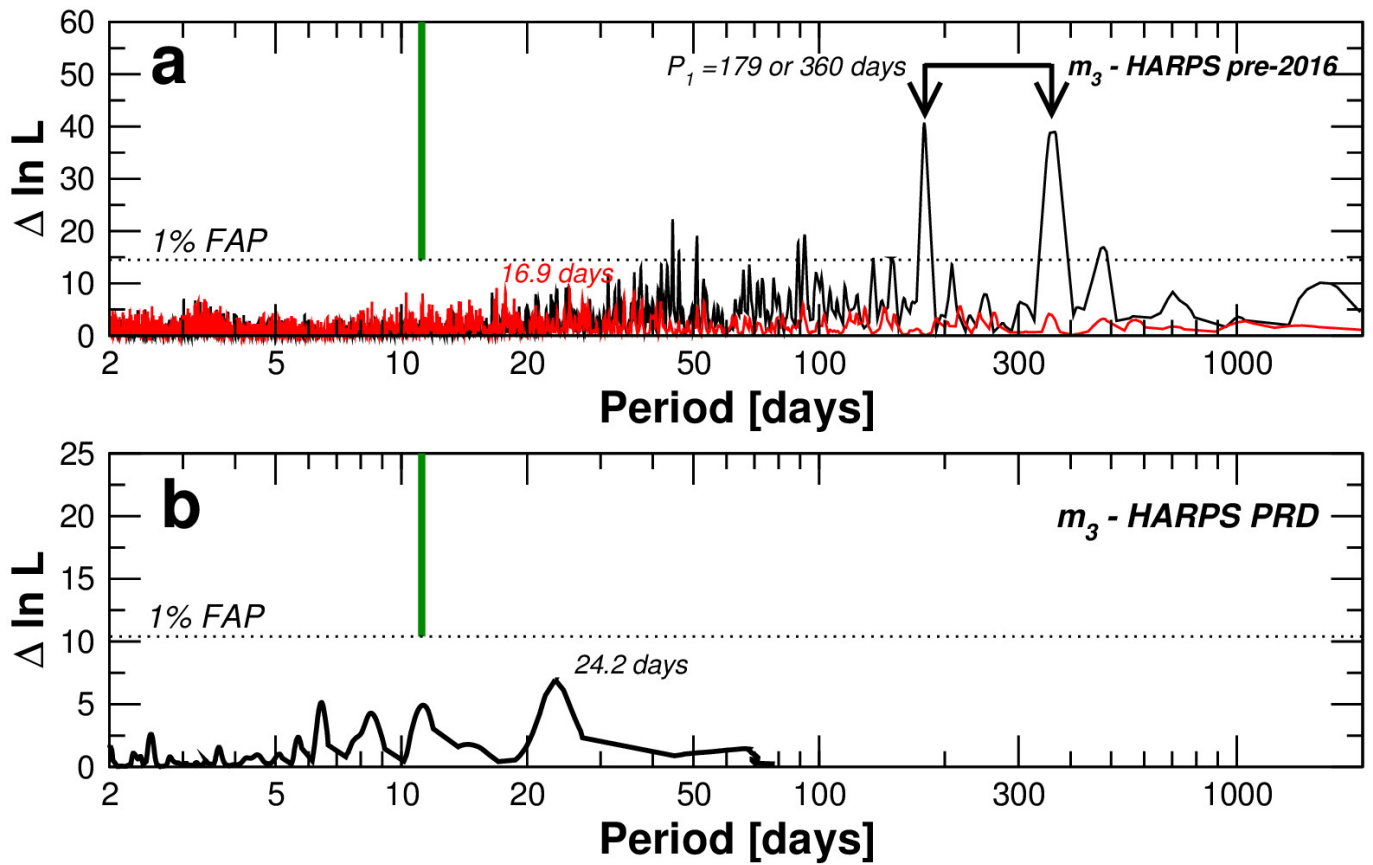
Extended Data Figure 3 | Signal searches on the photometry. a–d, Likelihood-ratio periodograms searches for signals in each photometric ASH2 photometric band (a, b) and LCOGT bands (c, d). The two sinusoid fits to the ASH2 S II series ($P_1 = 84$ d, $P_2 = 39.1$ d) are used

later to construct the FF' model to test for correlations of the photometry with the radial velocity data. The black, red and blue lines represent the search for the first, second and third signal respectively. The green vertical lines mark the period of the planet candidate at 11.2 d.



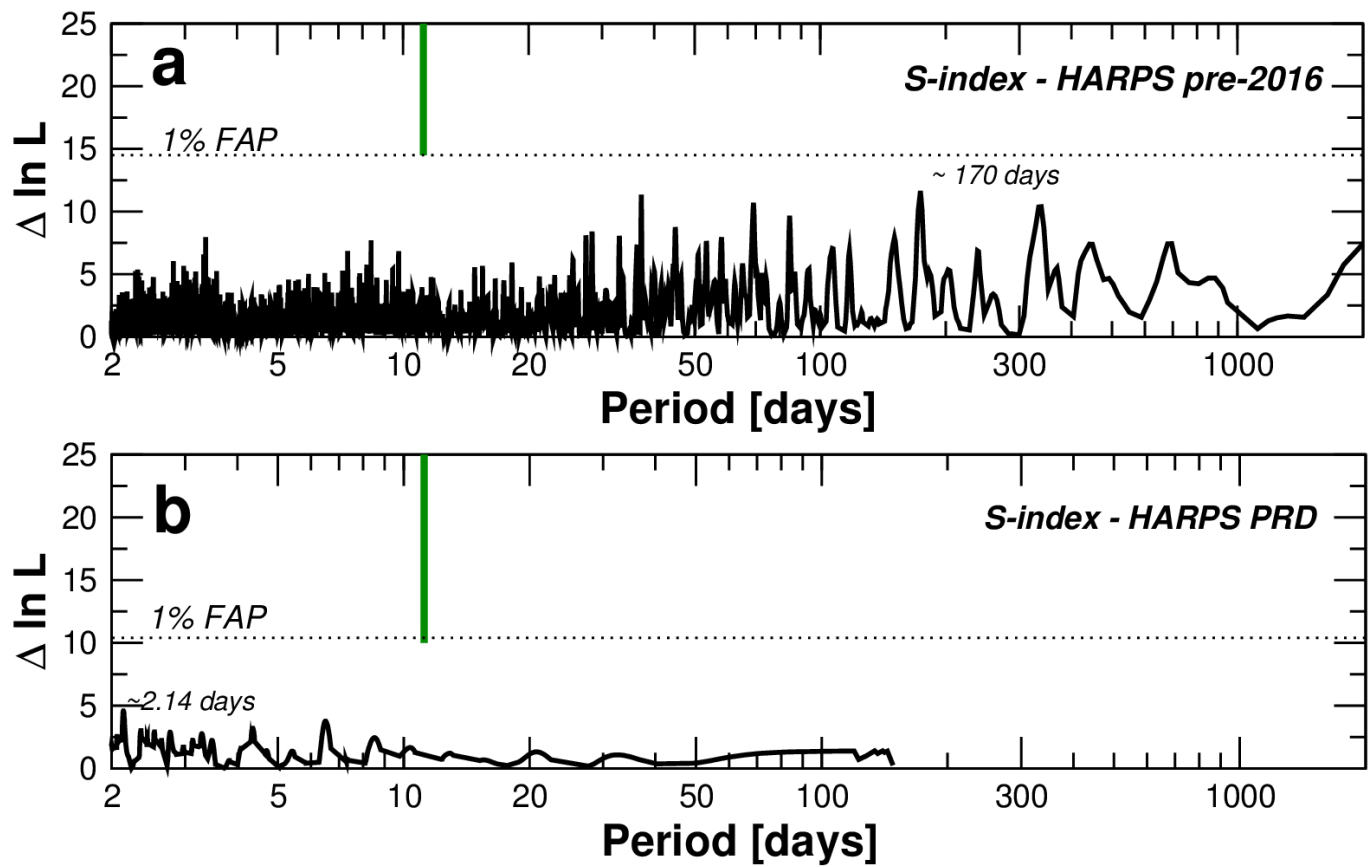
Extended Data Figure 4 | Signal searches on the width of the spectral lines. a, b, Likelihood-ratio periodogram searches on the width of the mean spectral line as measured by m_2 for the HARPS pre-2016 (a) and HARPS PRD data (b). The signals in the HARPS pre-2016 data are comparable to the photometric period reported in the literature and the

variability in the HARPS PRD run compares quite well to the photometric variability. The black, red and blue lines represent the search for the first, second and third signal, respectively. The green vertical lines mark the period of the planet candidate at 11.2 d.

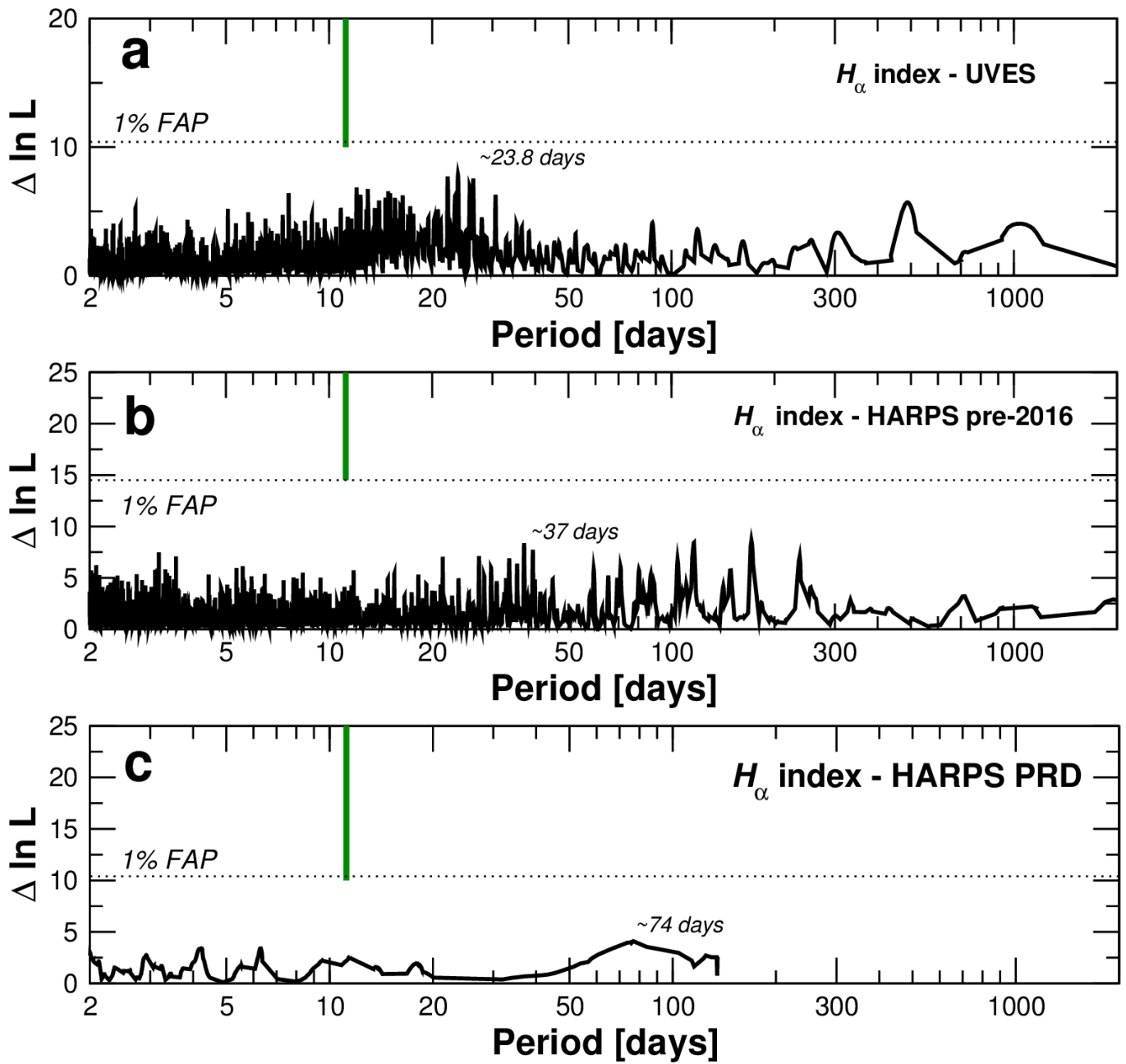


Extended Data Figure 5 | Signal searches on the asymmetry of the spectral lines. a, b, Likelihood-ratio periodogram searches on the line asymmetry as measured by m_3 from the HARPS pre-2016 (a) and HARPS PRD (b) data sets. Signal beating at around 1 yr and 0.5 yr is detected in the HARPS pre-2016 data, which is possibly related to instrumental

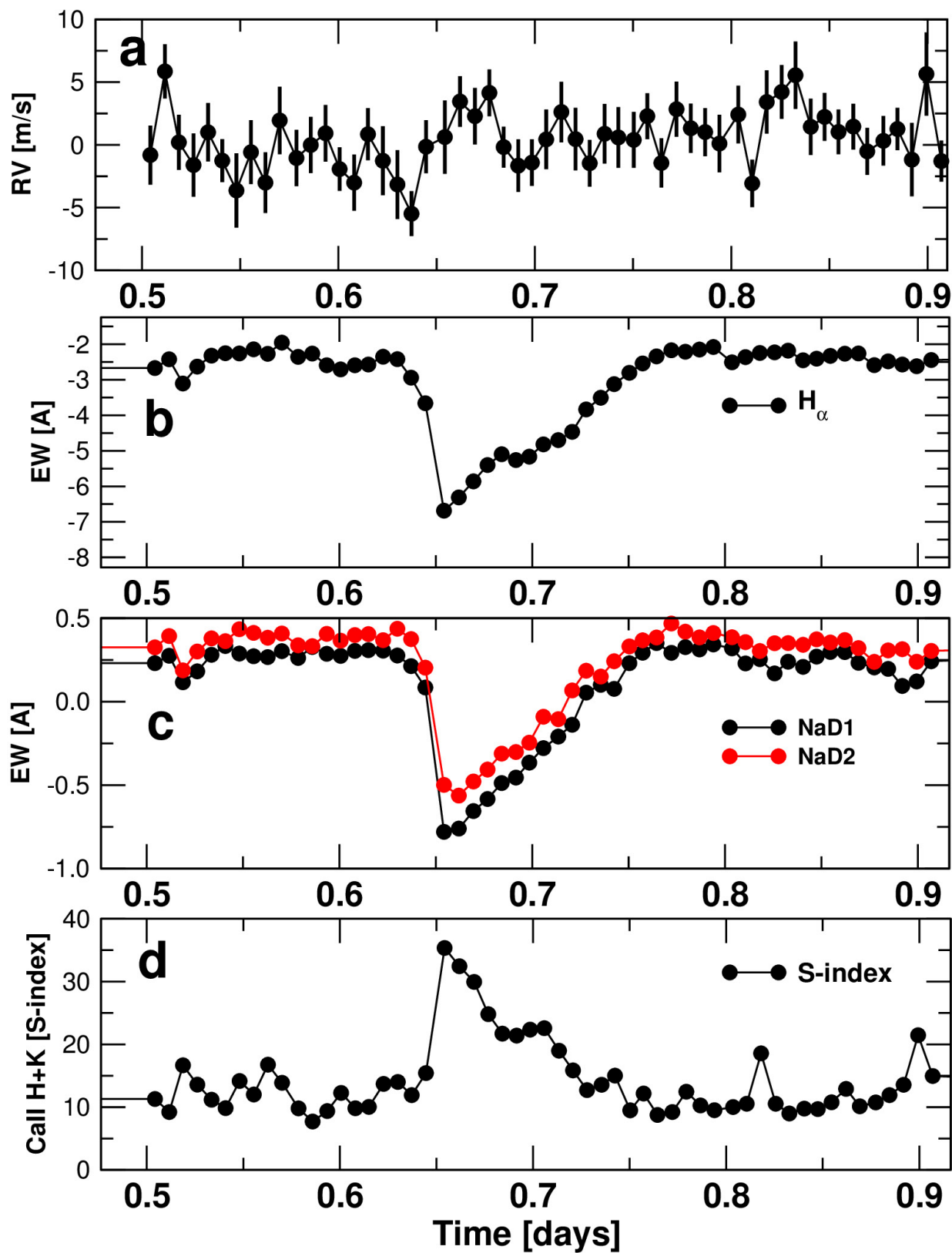
systematic effects or telluric contamination. No signals are detected above the 1% threshold in the HARPS PRD campaign. The black and red lines represent the search for the first and second signals respectively. The green vertical lines mark the period of the planet candidate at 11.2 d.



Extended Data Figure 6 | Signal searches on the chromospheric S-index. **a, b,** Likelihood-ratio periodogram of the S-index from the HARPS pre-2016 (a) and HARPS PRD (b) campaigns. No signals were detected above the 1% threshold. The green vertical lines mark the period of the planet candidate at 11.2 d.

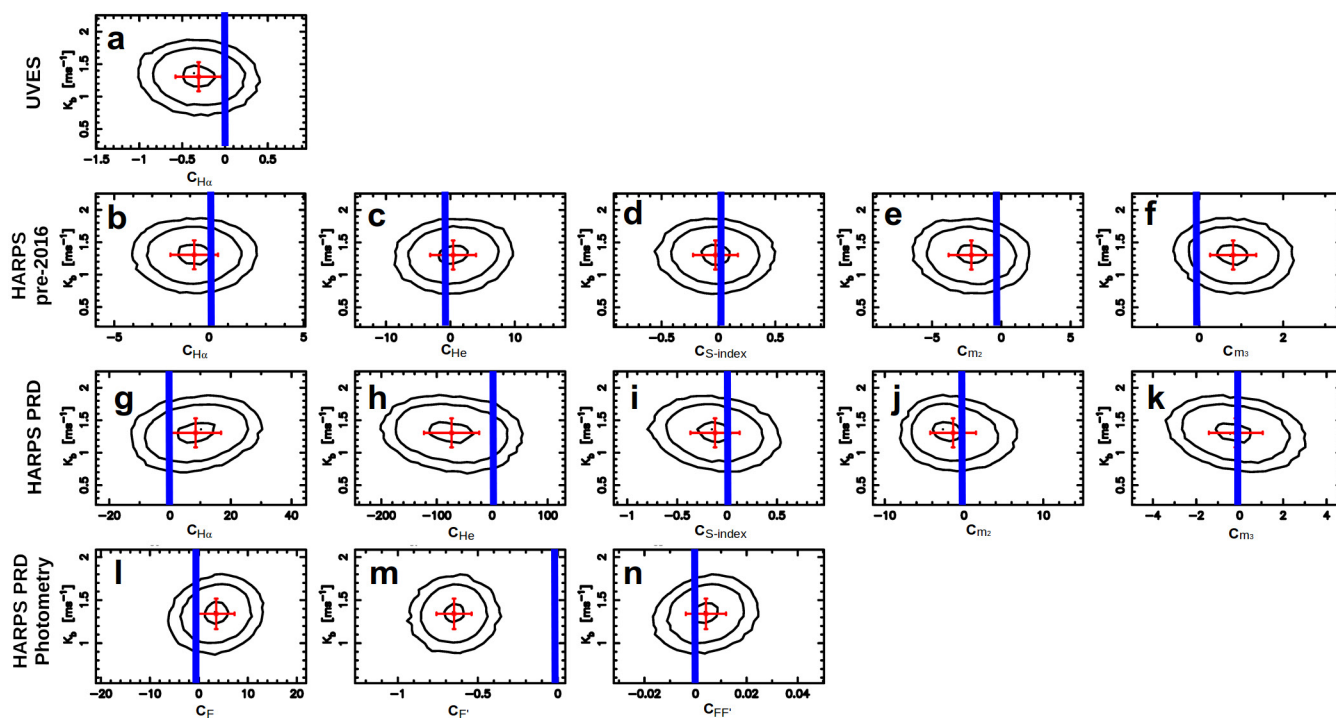


Extended Data Figure 7 | Signal searches on the spectroscopic H_{α} index. a–c, Likelihood-ratio periodogram searches of H_{α} intensity from the UVES (a), HARPS pre-2016 (b) and HARPS PRD (c) campaigns. No signals were detected above the 1% threshold. The green vertical lines mark the period of the planet candidate at 11.2 d.



Extended Data Figure 8 | Radial velocities and chromospheric emission during a flare. a–d, Radial velocities (a) and equivalent width measurements of the H α (b), Na doublet lines (c) and the S-index (d) as a function of time during a flare that occurred the night of 5 May 2013. The

time axis is days since JD = 245417.0 d. No trace of the flare is observed in the radial velocities. Error bars in the radial velocities correspond to 1σ errors. The formal 1σ errors in the equivalent width measurements are comparable to the size of the points.



Extended Data Figure 9 | Probability distributions for the activity coefficients versus the signal amplitude. a–n, Marginalized posterior densities of the activity coefficients versus the semi-amplitude of the signal for UVES (a), HARPS pre-2016 (b–f), HARPS PRD campaign (g–k) and the photometric FF' indices for the PRD campaign only (l–n). Each

panel shows equiprobability contours containing 50%, 95% and 99% of the probability density around the mean estimate, and the corresponding standard deviation of the marginalized distribution (1σ) in red. The blue bar shows the zero value of each activity coefficient. Only $C_{F'}$ is found to be substantially different from zero.

Extended Data Table 1 | Complete set of model parameters

Parameter	Mean [68% c.i.]	Units
Period	11.186 [11.184, 11.187]	days
Doppler Amplitude	1.38 [1.17, 1.59]	ms^{-1}
Eccentricity	<0.35	–
Mean Longitude	110 [102, 118]	deg
Argument of periastron	310 [-]	deg
Secular acceleration	0.086 [-0.223, 0.395]	$\text{ms}^{-1}\text{yr}^{-1}$
Noise parameters		
σ_{HARPS}	1.76 [1.22, 2.36]	ms^{-1}
σ_{PRD}	1.14 [0.57, 1.84]	ms^{-1}
σ_{UVES}	1.69 [1.22, 2.33]	ms^{-1}
ϕ_{HARPS}	0.93 [0.46, 1]	ms^{-1}
ϕ_{PRD}	0.51 [-0.63, 1]	ms^{-1}
ϕ_{UVES}	0.87 [-0.02, 1]	ms^{-1}
Activity coefficients*		
UVES		
$C_{\text{H}\alpha}$	-0.24 [-1.02, 0.54]	
HARPS pre-2016		
$C_{\text{H}\alpha}$	-0.63 [-4.13, 3.25]	
C_{He}	1.0 [-9.3, 11.4]	
C_{S}	-0.027 [-0.551, 0.558]	
C_{m_2}	-1.93 [-6.74, 2.87]	
C_{m_3}	0.82 [-0.60, 2.58]	
HARPS PRD		
$C_{\text{H}\alpha}$	9.6 [-12.9, 33.3]	
C_{He}	-77 [-210, 69]	
C_{S}	-0.117 [-0.785, 0.620]	
C_{m_2}	-2.21 [-8.86, 7.96]	
C_{m_3}	-0.02 [-3.67, 3.44]	
PRD photometry		
C_{F}	0.0050 [-0.0183, 0.0284]	
$C_{\text{F}'}$	-0.633 [-0.962, -0.304]	
$C_{\text{FF}'}$	4.3 [-6.8, 14.8]	

The definition of all of the parameters is given in Methods subsection 'Statistical frameworks and tools'. The values are the maximum *a posteriori* estimates and the uncertainties are expressed as 68% credibility intervals. The reference epoch for this solution is Julian Date $t_0 = 2,451,634.73146$ d, which corresponds to the first UVES epoch.

*The units of the activity coefficients are metres per second divided by the units of each activity index.